The Loosely-Bound Proton in ^{13}N and the Transfer Reaction ^{11}B(^{13}N,^{12}C)^{12}C

Richard J. Neal

Thesis submitted for the degree of Doctor of Philosophy

Department of Physics and Astronomy

University of Edinburgh

1997

Abstract

The radioactive nucleus ^{13}N ($t_{1/2}$ = 10 min, $J^{\pi} = \frac{1}{2}^{-}$) contains one loosely bound proton (S_p = 1.94 MeV) which can be considered to be bound to a core of ^{12}C. Taking advantage of the recent availability of beams of radioactive nuclei at Louvain-la-Neuve, Belgium, a beam of ^{13}N has been used to investigate the transfer reaction ^{11}B(^{13}N,^{12}C)^{12}C. Particle-γ coincidence data was taken, using the LEDA silicon strip array and BaF_2 modules, gating on the 15.11 MeV γ-decay from the $T = 1$ state in ^{12}C*. Two final states, corresponding to $^{12}C_{gs}$+^{12}C*(15.11 MeV) and ^{12}C*(4.44 MeV)+^{12}C*(15.11 MeV) have been observed and angular distributions have been measured for both transitions at each of two beam energies, 29.5 MeV and 45 MeV.

The results are discussed with special reference to the loosely bound nature of the valence proton in ^{13}N; the transfer reaction has been modelled using a DWBA code, with the ^{13}N ground state constructed as a mixture of states: a $p_{1/2}$ proton bound to $^{12}C_{gs}$, or a $p_{3/2}$ proton bound to $^{12}C^*_{2+}$ (4.44 MeV). Fits to the experimental data have been obtained using a very shallow set of optical potentials, which are found to be energy dependent. The agreement with experiment is good, with the exception of the ^{12}C*(4.44)+^{12}C*(15.11) transition at the lower beam energy, which is significantly under-estimated by the calculations, suggesting a contribution from a different reaction mechanism.

Declaration

The experiments described in this thesis were carried out by myself and fellow collaborators. The theoretical simulations are my own work except where indicated otherwise. The data analysis and interpretation is my own work and this thesis has been written by myself.

Richard Neal

Acknowledgements

My first thanks must go to my supervisor, Alan Shotter, who has been a source of great help and advice on this project. Thanks are also due to Tom Davinson and my second supervisor Phil Woods, for their support.

Our collaborators in Belgium, especially Wilfried Galster, Alain Ninane, Csaba Sükösd and Pierre Leleux, should also be mentioned, for their contribution, crucial to this work, of a radioactive beam and support for its operation.

James Christley, Jim Al-Khalili and Ian Thompson are thanked for useful discussions on the theoretical aspect of the work, and especially for the initial calculations.

The Engineering and Physical Science Research Council (EPSRC) are thanked for funding this PhD project.

Finally, thanks go to my friends and family for providing support outside work, which has made my time in Edinburgh so enjoyable. Good luck to Martin O'Neill and to E=M.C.C. - you did us proud.

Contents

List of Figures

List of Tables

Chapter 1

Introduction

1.1 Radioactive Nuclear Beams

Nuclear physics has long been limited by the number of accessible entrance channels to nuclear reactions, due to the practicalities of bringing together a particular projectile-target combination in reasonable quantities. This has meant using beams of stable nuclei and stable or long-lived targets. However, in recent years the availability of beams of relatively short-lived radioactive nuclei has made it possible to study a great number of new reactions which previously were inaccessible or only indirectly observable. These include many that yield information about astrophysical processes such as fusion in stellar interiors, which can depend on sequences of reactions which proceed *via* unstable nuclei. For example, the sequence $^{15}\mathrm{O}(\alpha,\gamma)^{19}\mathrm{Ne}(\mathrm{p},\gamma)^{20}\mathrm{Na}$ is part of the transition from the hot Carbon-Nitrogen-Oxygen (CNO) cycle to the rp-process, and the use of a radioactive beam has made it possible to place limits on the reaction rate of $^{19}\mathrm{Ne}(\mathrm{p},\gamma)^{20}\mathrm{Na}$ [1]. Reactions that are of interest purely to nuclear physics itself can also be directly accessed for the first time; the ^{13}N beam at Louvain-la-Neuve has been used to directly populate the 7.77 MeV state in ^{14}O, to investigate the possibility of diproton decay [2]. ^{13}N itself is the mirror nucleus of ^{13}C, and as such is of interest

in one of the fundamental concepts of nuclear physics, the charge-independence of the nucleon-nucleon force. Charge symmetry in heavy ion reactions has been difficult to investigate because most pairs of mirror nuclei contain a short-lived nucleus.

There are also potential applications for radioactive nuclear beams in areas outside pure physics, such as the medical and environmental sciences [3].

The experiments discussed in this thesis take advantage of the newly available radioactive beams, specifically ^{13}N, a radioactive isotope with a half-life of 10 minutes.

ISOL and IFS Radioactive Beam Production

There are two ways of producing a radioactive ion beam that are currently employed in various facilities around the world. Both involve a primary, stable beam on a target, suitably chosen for a high yield of the required radioactive product. In-Flight Separation (IFS) facilities employ the break up of the beam nuclei, in a thin production target from which the beam-like fragments emerge, to be mass-separated to select the desired nuclei, giving a secondary beam of the unstable isotope.

The principle difference between IFS and Isotope Separation On-Line (ISOL), the second method of producing a radioactive beam, is that in the latter the reaction products from the primary beam and the production target are stopped, either in a separate catcher or in the thick production target itself, before being re-accelerated. The unstable atoms are ionised, mass-separated, and finally accelerated to the desired energy by a second cyclotron. This is the method used at the radioactive beams facility at Louvain-la-Neuve, Belgium, where the experiments described here were carried out. A primary beam of 30 MeV protons is used with a suitable production target, making beams of light proton rich nuclei such as

^{19}Ne and ^{13}N. Details of the beam source at Louvain-la-Neuve can be found in Chapter 2.

Figure 1.1 shows the major features of ISOL and IFS beam sources. Reference 4 is a general review of the techniques used in IFS and ISOL facilities.

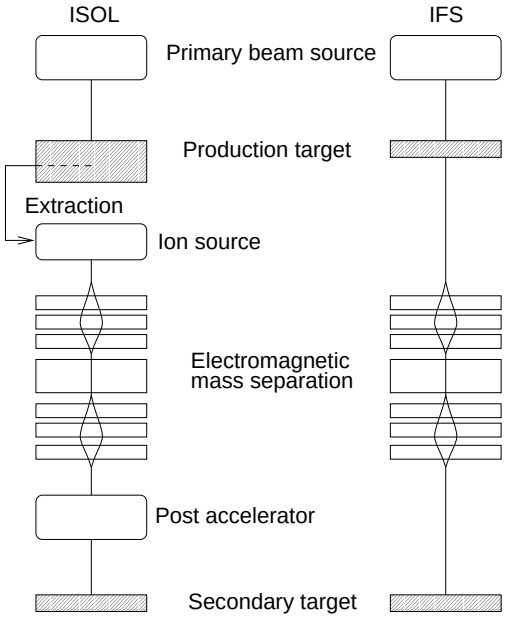

Figure 1.1: *ISOL and IFS production of radioactive ion beams*

1.2 Halo and Skin Nuclei

Radioactive beams of proton- or neutron-rich species have opened up new opportunities to study a group of nuclei that have attracted a great deal of interest recently. The so-called halo nuclei are said to have a structure based on an inert core nucleus and one or more loosely bound nucleons with highly extended wave functions, making a 'halo' around the central core. The best known and most studied halo nuclei are ^{11}Be and ^{11}Li; table 1.1 lists some other halo nuclei and candidates for halo status, and their halo-core composition.

The term 'halo' was originally coined to describe nuclei with a larger than normal

Nucleus	E_{ex} (MeV)	Structure
^{11}Be		n+^{10}Be
^{11}Be*	0.32	n+^{10}Be
^{14}Be		n+n+^{12}Be
^{11}Li		n+n+^{9}Li
^{6}He		n+n+^{4}He
^{17}F*	0.50	p+^{16}O
^{8}B		p+^{7}Be
^{17}Ne		p+p+^{15}O

Table 1.1: *Some halo nuclei and other candidates*

neutron density distribution [5]. However, the consensus today seems to be to refer to such cases as a neutron skin, as distinct from an abnormally strong tail in a nucleon wave function, and halos exist at the limits of stability, whereas neutron skins can be found in less extreme cases. The spatial extension of the halo gives rise to enhanced total reaction cross sections (as does a neutron skin) but the properties of the core are largely unaffected by the presence of the halo; this behaviour is illustrated by the results reported by Blank *et al* [6] and shown in figure 1.2).

This work compares the reactions of ^{8,9,11}Li at 80 MeV/nucleon on carbon; the total reaction cross sections (σ_{tot}) were measured along with those for charge-changing processes (σ_{cc}; *ie* reactions on the core). It was found that σ_{cc} was almost the same for each isotope of lithium, whereas σ_{tot} was rather larger for the halo nucleus ^{11}Li. The conclusion is that the proton distribution in ^{11}Li is not affected by the long tail in the neutron distribution. In contrast, a neutron skin is viewed as being simply a state where the neutron mass distribution extends further than that of the protons. Halos are thought to be characterised by a more granular structure; in a skin, the neutrons are uncorrelated with other, but two-neutron halos show a close correlation between the two neutrons and the core.

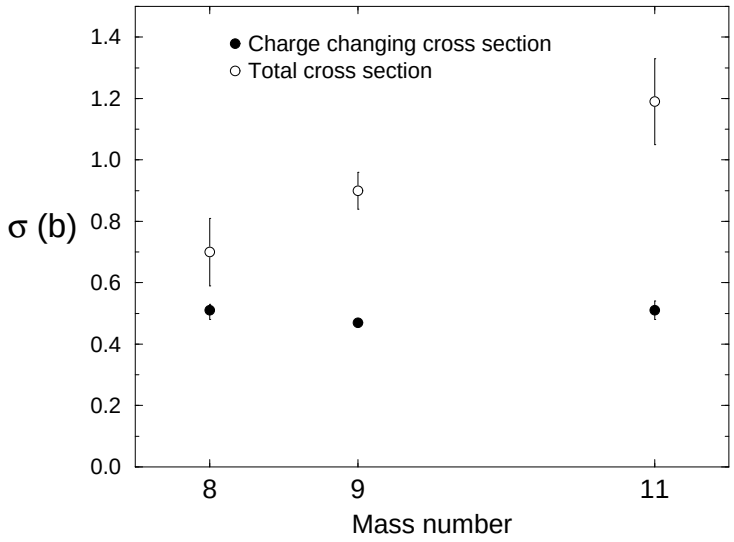

Figure 1.2: *Charge-changing and total reaction cross sections of lithium on carbon, after Blank* et al

The halo can often be uniquely stable; for example, ^{9}Li is bound, and ^{11}Li is a bound two-neutron halo nucleus, but ^{10}Li is unbound—the one-neutron halo does not exist in lithium. Two-neutron halo nuclei such as ^{11}Li that do not have a bound one-neutron counterpart have been dubbed 'Borromean' [7], after the heraldic Borromean Rings—if any one of the 'rings' in the ^{9}Li+n+n system were removed the others would fall apart. For nuclei with a neutron skin, however, adding extra neutrons simply extends the neutron distribution further; figure 1.3 shows the mean neutron radii for $^{20-32}$Na, from work published by Suzuki *et al* [8].

Many other examples of neutron skins exist, and it has been suggested that proton skins might exist in ^{100}Sn [9] and ^{20}Mg [10], for example. There has been a suggestion, in fact, that all β-unstable nuclei will have a neutron or proton skin to some degree. However, definitions of the distinction between a skin and a halo are often the source of debate when applied to certain nuclei; ^{6}He has been called a halo nucleus, and a Borromean one at that (^{5}He is unbound), but experimental results and theoretical considerations have been reported [11] that lend support

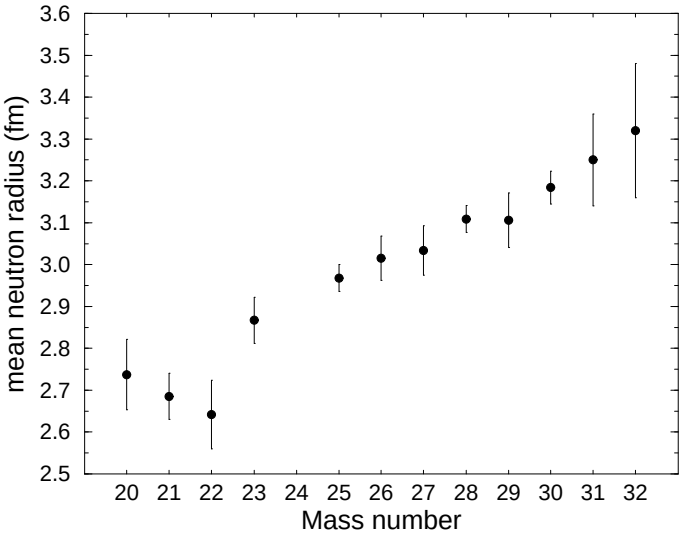

Figure 1.3: *Neutron radii of sodium isotopes*

to the claim that it sports a neutron skin rather than a halo.

Several reviews of theoretical and experimental work on halo nuclei have been published, for example refs. 12, 13. However, most of the work published to date has concerned neutron halos, with a few exceptions. The 0.6 MeV excited state of ^{17}F* is regarded as a proton halo nucleus, and is involved in the breakout from the hot-CNO cycle, *via* proton capture by ^{16}O. ^{17}Ne is a candidate for a two proton halo [14], and it has been suggested [15] that ^{8}B contains a proton halo. The structure of this isotope also has astrophysical implications; in the solar neutrino model the β^+ decay of ^{8}B is a source of neutrinos.

1.3 ^{13}Nitrogen

^{13}N is another nucleus involved in the CNO cycle. It is also an interesting isotope in itself as the mirror nucleus of the stable ^{13}C and because it is one proton up from ^{12}C, with a low proton separation energy (S_p = 1.94 MeV). It might therefore be

useful to model ^{13}N as being a ^{12}C core with an extra proton—certain properties might be easier to explain if the proton could be viewed as being in a shell model type state, in the central potential of the ^{12}C core. The most straightforward way to study the "extra" proton would be in a single step transfer reaction, leaving the residual ^{12}C nucleus unaffected.

1.3.1 A model of ^{13}N

If ^{13}N is considered to be composed of a ^{12}C core in its ground state ($J^\pi = 0^+$), with a valence proton in a single particle state, that proton will occupy the next sub-shell, in a $1p_{\frac{1}{2}}$ state, giving the spin-parity ($\frac{1}{2}^-$) of $^{13}N_{gs}$. However, a number of other combinations of core plus proton states are possible and a superposition of these states should be considered. For example, the next such combination is a $1p_{\frac{3}{2}}$ state coupled with a ^{12}C in its first excited state, 2^+ at 4.44 MeV. Thus we have

$$|\Phi(^{13}\mathrm{N})\rangle \;=\; \alpha|^{12}\mathrm{C}(0^+)\otimes 1p_{\frac{1}{2}}\rangle \;+\; \beta|^{12}\mathrm{C}(2^+)\otimes 1p_{\frac{3}{2}}\rangle \;+\; \ldots \qquad (1.1)$$

Comparatively little work has been published on the ground state of ^{13}N, because of the difficulty of using unstable nuclei in heavy ion reactions. Clues as to its structure have been taken from measurable properties such as the nuclear magnetic moment and its β^+ decay. Excited states have been investigated with (p,γ) reactions on ^{12}C [16, 17], and Zucchiatti *et al* [18] has reported evidence of excited states with shell model structure consisting of a proton bound to a ^{12}C core, and also states where the carbon core is in the 2^+ first excited state. The structure of the mirror nucleus ^{13}C has, in contrast, been the subject of a great deal of discussion (see ref. 19 and references therein). This nucleus can also be modelled as a ^{12}C core plus nucleon (in this case, a neutron; $S_n = 4.95$ MeV). The evidence of various experimental and theoretical studies has often been in disagreement on the question of the amount of configuration mixing, *ie* the relative values of the coefficients α, β *etc.* The early work of Cohen and Kurath [20, 21]

gives wave functions that are dominated by the $p_{1/2}$ state. However, some experimental work has been interpreted as being in disagreement with this picture, particularly the pion charge exchange reaction $^{13}C(\pi^+, \pi^0)^{13}N$, and pion photoproduction $^{13}C(\gamma, \pi^-)^{13}N_{gs}$. The calculations of Singham [22, 23] are constrained by the experimental measurements of the magnetic dipole moments of ^{13}C and ^{13}N, the value of $\log ft$ for the β^+ decay of ^{13}N, and fits to the elastic scattering of electrons, data with which the Cohen-Kurath wave functions are less consistent. The Singham wave functions contains a considerable contribution from the $p_{3/2}$ state.

In the case of ^{13}N, a couple channels bound state calculation [24] carried out by Nunes suggests that the $p_{3/2}$ state is an important part of the ground state structure, with $|\alpha|^2 = 0.3195$ and $|\beta|^2 = 0.6704$; the contribution from any other proton states is thought to be negligible.

The different energy states of the ^{12}C core means that the kinematics of a reaction involving the direct one step transfer of a single proton to a target nucleus will be different for each case; events where the exit channel contains a 2^+ $^{12}C^*$ would de-excite *via* γ-decay, and the two core states could in principle be distinguished either by observing the γ-photon, or from the different Q-values. The spectroscopic factors $|\alpha|^2$ and $|\beta|^2$ could also in principle be measured from the relative cross sections, if the reaction mechanism could be accurately modelled.

1.3.2 Comparison to ^{13}C

The similarity between ^{13}N and ^{13}C, and the charge-symmetry of the nuclear interaction should give them similar properties as in many respects. Liénard *et al* [25] have compared the elastic scattering of ^{13}N and ^{13}C on ^{12}C in experiment and theory. Optical model fits are obtained for the scattering of ^{13}C, and the same parameters, with the imaginary depth replaced by one shallower by a factor

of between $\frac{1}{3}$ and $\frac{1}{5}$, fit the ^{13}N data well. The theoretical treatment of the elastic cross sections in this work includes a parity dependent term $(-)^l V_p$, which depends on the parity of each particular partial wave and on whether the valence nucleon is a proton or neutron (because of the effect of the Coulomb interaction). This term is included as a consideration of the elastic transfer [26–28], where the least bound nucleon transfers between the two identical ^{12}C cores, causing the cross section to rise at backward angles (see Chapter 4). This effect is larger in ^{13}N, because the Coulomb repulsion between the core and the proton means that it is less bound than the neutron in ^{13}C.

1.3.3 Single Particle Transfer on ^{11}B

A favourable reaction involving the valence proton in ^{13}N is the transfer of a proton to ^{11}B, giving ^{12}C+^{12}C. Observing this reaction directly has thus far been impracticable; a target of ^{13}N cannot be used because of its relatively short half life, but ^{13}N beams are available at Louvain-la-Neuve, and ^{11}B is stable. Figure 1.4 shows the ground state of ^{13}N in relation to ^{12}C plus proton, of ^{12}C in relation to ^{11}B plus proton, and some of the excited states of ^{12}C.

Assuming that the ^{12}C core is inert as far as the transfer reaction is concerned, its initial state, as well as the possible excitation of the recoil carbon, will determine the Q-value, and thus the kinematics of the reaction. The cross section of nucleon transfer is also dependent on the Q-value of the reaction. Q-matching [29, 30] requires that, in semi-classical terms the change in linear and angular momentum experienced by the transferred nucleon or cluster should be small, so that the transition should be as 'smooth' as possible (fig 1.5). The Q-value and the beam energy determine how well matched the reaction is, and for a poorly matched reaction the cross section will be suppressed; the relative cross sections of the 0^+ and 2^+ states will therefore be dependent on the beam energy.

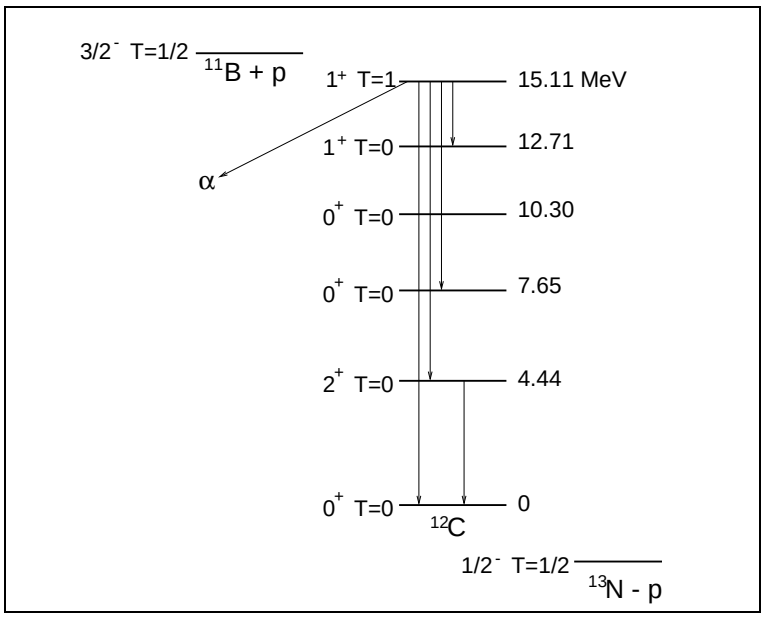

Figure 1.4: *Energy levels of* ^{13}N,^{11}B *and* ^{12}C

There are several recipes for determining the optimum Q-value, Q_{opt}, depending on the assumptions made and the nature of the reaction, and calculations of Q_{opt} must be treated cautiously since they either neglect the effect of the nuclear potential or depend on estimates of it, and also on estimates of the nuclear radii, which carry a degree of uncertainty. The various models can however sometimes be successful in explaining why a particular reaction preferentially populates specific states. A summary of the different Q_{opt} models is given by Bass [31, page 147].

The model proposed by Siemens *et al* [30] assumes that

1. The transferred nucleons leave the donor nucleus without losing any of their individual momenta.

2. The nucleus to which the nucleons are transferred is able to absorb them freely and accept their momentum.

3. The transferred nucleons are at rest with respect to the donor nucleus.

Under these conditions, we have equation 4.40 in ref. 31:

$$Q_{opt} = -E_{CM}\left[(1-\gamma_V) + (\gamma_L - \gamma_V)\xi + \frac{1}{2}(\gamma_L - \gamma_V)^2\xi(1-\xi)\right] \qquad (1.2)$$

$$(1-\gamma_L) = \frac{Mm_x}{(M_1+m_x)(M_2+m_x)} \qquad \gamma_V \approx \frac{Z_1(Z_2+z)}{(Z_1+z)Z_2} \qquad \xi \approx \frac{2\sin\frac{\theta}{2}}{1+\sin\frac{\theta}{2}}$$

... where m_x and z are the mass and charge of the transferred particle and M_1, M_2 and Z_1, Z_2 are the masses and charges of the core nuclei.

The experiments described in this thesis were performed above the Coulomb barrier (around 8 MeV) at beam energies 29.5 and 45 MeV in the lab (13.5 and 20.6 MeV in the centre of mass). At these energies, for $\theta = 5^o$ (*ie* inside the grazing angle), (1.2) gives $Q_{opt} = -1.8$ MeV and -2.8 MeV respectively; if a state in ^{12}C+^{12}C existed for which the transfer had Q-value close to these values of Q_{opt}, then we would expect that state to be favourably populated. The ground state of ^{11}B plus the mass of a proton is very close to the state at 15.11 MeV in ^{12}C; a transition to this state could be identified by observing the gamma decay to the ground state. The Q-values for ^{11}B(^{13}N,^{12}C$_{gs}$)^{12}C$^*_{15.11}$ and ^{11}B(^{13}N,^{12}C$^*_{4.44}$)C$^*_{15.11}$ are -1.18 MeV and -5.62 MeV respectively. The former case appears to quite well matched at the lower beam energy, but for the latter transition the higher energy is more suitable, according to this recipe.

1.4 The Present Work

The aim of this work has been to identify the transfer reaction on ^{11}B, and to measure the cross sections for the two different final states in ^{12}C$^{(*)}$+^{12}C*. It is further intended to use a theoretical code based on direct reaction theory to model the transfer reaction, and reproduce the experimental data, making the assumption that the origin of the two states in the exit channel is to be found in the mixed configuration of the ground state of ^{13}N.

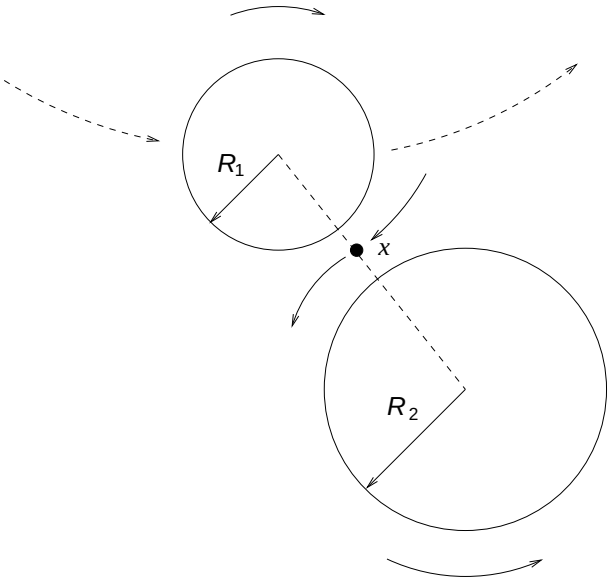

Figure 1.5: *Semiclassical picture of a transfer reaction taking place in the scattering plane at distance of closest approach, after Brink [29].*

This thesis will describe the experiments which have been carried out to measure the transfer reaction on ^{11}B, and the theoretical interpretation of the experimental data. Chapter 2 gives details of the experimental procedure, describing the detector setup and the instrumentation used. Chapter 3 will discuss the analysis of the data obtained in the three experimental runs; how the transfer reaction events were extracted, and how the angular distributions were derived from those events. Chapter 4 then discusses the code that was used to model the reaction; it is attempted to reproduce the experimental results in the framework of direct reaction theory, modelling the reaction as a one step quasi-elastic process. Chapter 5 goes on to review the success of the calculations in predicting the cross sections, and discusses ways in which any discrepancies might be explained. Possible future investigations which follow on naturally from the present work and the questions it raises are also considered.

Chapter 2

Experimental Procedure

The experimental work was carried out at the ARENAS[3] facility at Louvain-la-Neuve using silicon strip arrays, to detect charged particles, in conjunction with an array of barium fluoride crystals, to detect coincident gamma rays.

2.1 Production of ^{13}N beam

The ^{13}N beam used in these experiments is produced *via* a (p,n) reaction with the 30 MeV proton beam from the cyclotron CYCLONE 30 on a target [32] of 99% enriched ^{13}C. The yield of ^{13}N from a thick ^{13}C target (in this case, around 1 g/cm^2) at 30 MeV is 1.6×10^{-3} per proton [33], and with a typical proton current of 150 μA this gives a rate of production of 1.5×10^{12} particles per second.

The ^{13}N is extracted by flushing the production target, which is heated by the primary beam to 2000 K, with nitrogen gas, and the radioactive nitrogen emerges in the form of ^{13}N-^{14}N molecules. The efficiency of extraction of ^{13}N from the production target is around 20–30 %. The radioactive nitrogen gas is then passed to an Electron Cyclotron Resonance (ECR) ion source [34], which operates at $\sim$7 kV and is optimised for production of ions at the low charge states (+2 for

the 29.5 MeV beam, and +3 at 45 MeV) at which the beams are accelerated. Efficiency of extraction from the ECR source is around 40 %. The ions are then mass-separated by a 90° analysing magnet and passed to the post-accelerator CYCLONE, a $K = 110$ cyclotron operating in harmonic 6 or 3, allowing beam energies up to 0.6 or 9 MeV/nucleon respectively. The efficiency of transport through the post accelerator is 3–5 %, giving a final beam current of $\sim 10^9$ pps, or 100 ppA.

Figure 2.1 illustrates the layout of the primary beam, production target, and post-accelerator.

2.2 Detection System

The reactions studied in these experiments were detected with silicon strip p-n junction devices, for charged particles, and an array of BaF_2 scintillator detectors, for gamma rays.

2.2.1 Silicon Strip Detectors

Silicon has a number of advantageous characteristics that mean it is widely used as a material for detecting ionising radiation. The low band gap at room temperature (1.1 eV), high electron and hole mobilities and high minority charge carrier life times mean that noise and timing characteristics of silicon detectors are very favourable. The high intrinsic resistivity of silicon (2.3×10^5 Ωcm) also makes such devices more practical than, for example germanium which has a lower resistivity (47 Ωcm) and therefore a higher dark current and needs to be cooled to liquid nitrogen temperatures for optimum performance [35, 36].

Figure 2.2 shows a basic p-n junction.

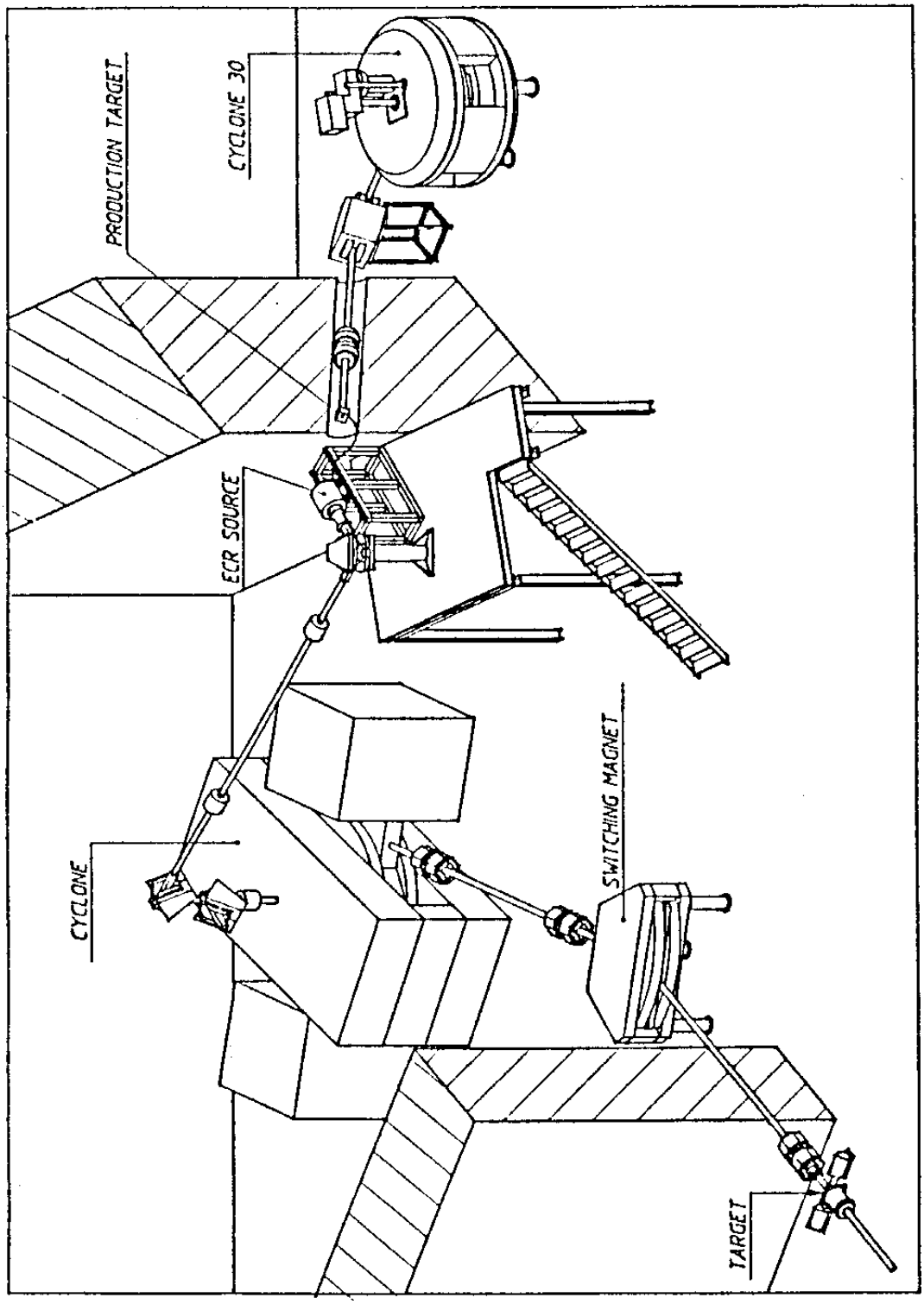

Figure 2.1: *Radioactive beam production at Louvain-la-Neuve*

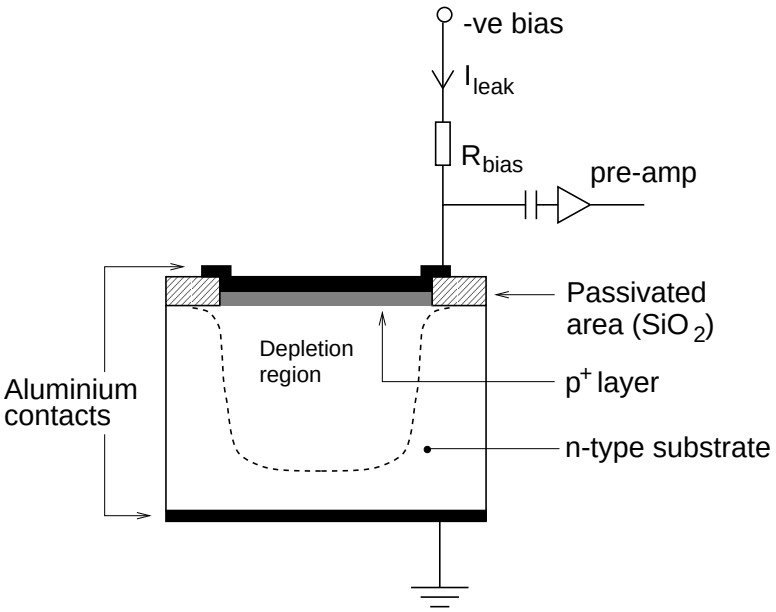

Figure 2.2: *A p-n junction*

The p-n junctions are operated under reverse bias, a negative potential applied to the p^+ face *via* a thin aluminium contact. This produces a depletion region across most of the thickness of the silicon—which is important if the total charge deposited by a particle is to be collected; the lower energy or higher mass particles will be stopped near the front of the detector, but protons punch through 300 μm of silicon (the thickness of detector used in these experiments) at only 6 MeV initial energy, and alphas at 24 MeV. To ensure depletion across the whole volume of silicon, these devices are usually operated at bias voltages much higher than the theoretical depletion voltage. The depletion region is the active detector volume—ionising radiation incident on this volume creates highly mobile charge pairs, which move under the electric field to generate a current pulse. Except under the influence of ionising radiation, there are, ideally, no mobile charges in the depletion region and what small leakage current exists is due to impurities and defects in the device contributing electrons to the conduction band *via* thermal excitation.

Recent developments in the semiconductor industry have made it possible to fab-

ricate large numbers of p-n junction diodes on a single silicon wafer, making available highly segmented, large area detectors. Double sided strip detectors, with the p^+ and n^+ sides divided into two sets of orthogonal strips are commonly used today; these provide very high spatial resolution, since an event in a p^+ strip accompanied by an equal energy event in an n^+ strip can be located in pixel defined by the intersection of the two strips. These detectors can be used for high multiplicity coincidence experiments, or in work where higher spatial resolution is necessary, or simply when a large detector is needed to cover as much solid angle as possible. Leakage current between strips is minimised by passivating the inter-strip region; this small dead area is oxidised at very high temperature.

LEDA

The Louvain-Edinburgh-Detector-Array (LEDA) (fig. 2.2.1), fabricated by Micron Semiconductors [37] is a large area annular silicon strip detector, made of eight segments, each with sixteen p^+ strips on the front face. The back face of each segment is a single n^+ element. The front and back faces have a 0.3 μm thick aluminium contact for the application of the bias voltage, typically 80 V. The inter-strip separation is 100 μm, compared to a strip width of 5 mm, so the dead area between strips is minimal.

In the experiments described here, only the front strips were used. Each strip was separately instrumented, allowing multi-particle coincidence events to be recorded. The pre-amps and shaping amps used with the LEDA segments were designed by the Edinburgh nuclear physics group and the Rutherford Appleton Laboratory [38, 39], with the aim of providing compact and cheap instrumentation of the large numbers ($ie > 100$) of detector channels that silicon strip detectors provide.

Each LEDA segment had a pre-amp box mounted on the outside of the reaction chamber, containing a motherboard on which was mounted 16 of the modular pre-amp cards. The amplifiers were similarly modular; a single module contained

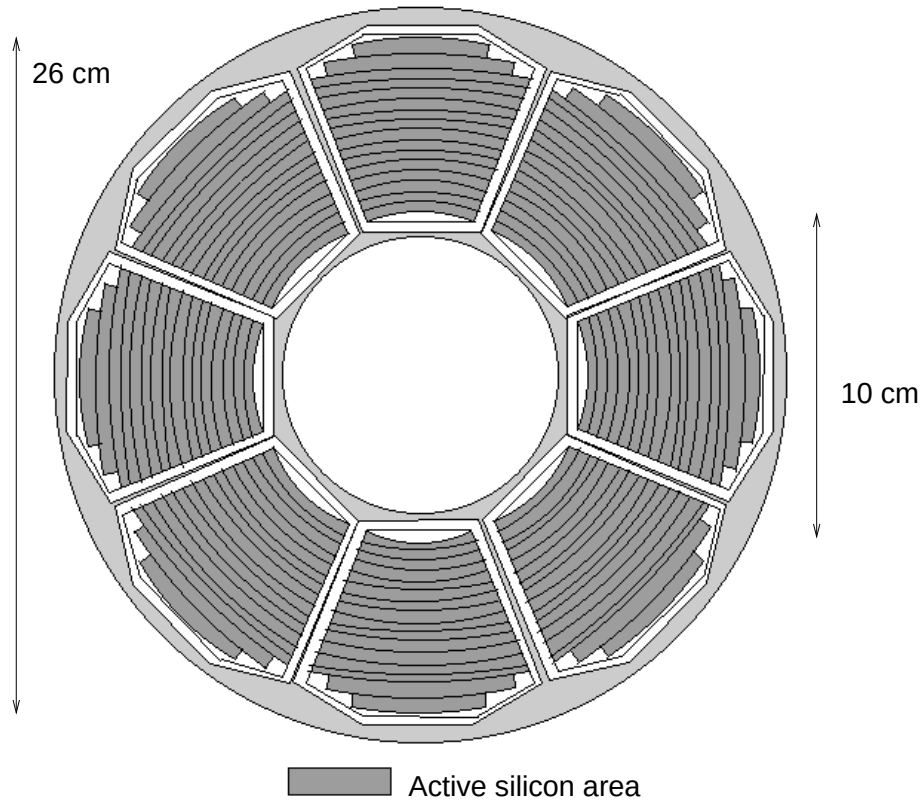

Figure 2.3: *LEDA*

Thickness	300μm	Inner diameter		10 cm
Active area	56 cm^2	Outer diameter		26 cm
Strip width	5 mm	$\Delta\theta$	(strip 0, outermost)	19^o
Inter-strip distance	0.1 mm		(strip 1)	29^o
Thickness of Al contact layer	0.3 μm		(strip 2)	37^o
Thickness of p$^+$ layer	0.1 μm		(strips 3–15)	43^o

Table 2.1: *Dimensions of one LEDA segment*

eight cards, each with a shaping amplifier and discriminator circuit. The amplifier modules gave two outputs for each channel, an analogue output to be sent to the ADCs, and a logic ECL output, used in the trigger electronics. The gain of the amplifiers was set by interchangeable resistor packs; for the runs with beam energy 29.5 MeV, 1 kΩ resistor packs were used, giving a full range (9.375 V in the ADC) of ∼40 MeV. For the experiments at 45 MeV the energy range was ∼70 MeV, with 2.7 kΩ resistors.

2.2.2 Gamma Ray Detection - BaF_2

Gamma rays were detected in these experiments with modules of a scintillator, BaF_2 , with photomultiplier tubes.

Properties of Barium Fluoride

As a scintillator, BaF_2 is rather insensitive to radiation damage [40,41] and energy resolution in the range 2–50 MeV is comparable [42–46] to other materials such as NaI or BGO. Another advantage of BaF_2 over other inorganic scintillators is that it is not hygroscopic, which makes it easier to handle, and it is very temperature-stable [47]. It also has the advantage of good time resolution, typically less than 0.5 ns. This is a consequence of a fast component [48] in the emission spectrum at around 220 nm that accompanies the slower response typical of other inorganic scintillators. This fast pulse allows particle identification in principle; the relative intensities of the two emission components are dependent on the type of particle, and the fast pulse is very suppressed for charged particles compared to gammas. The fast pulse was used in these experiments for the trigger logic, but since the crystals were mounted outside the reaction chamber, the rate of charged particles was expected to be negligible. Charged particle discrimination was therefore not necessary here.

Table 2.2 shows the physical properties of BaF_2 and some other commonly used scintillators; see also ref. 36, pages 239–271.

	BaF_2	CsI(Tl)	CsF	NaI(Tl)	BGO[a]
Peak emission (nm) (slow)	**310**	540	-	415	505
Peak emission (nm) (fast)	**220**	-	390	-	-
Decay time (ns)	**0.6**	1000	4	230	300
Photons/MeV	**10000**	52000	∼3000	38000	8000
Density (g/cm^3)	**4.88**	4.51	4.11	3.67	7.13
Refractive index	**1.49**	1.80	1.48	1.85	2.15
Hygroscopic	**No**	Yes	Yes	Yes	No

[a]Bismuth Germanate, $Bi_4Ge_3O_{12}$

Table 2.2: *Physical characteristics of barium fluoride and other scintillators*

BaF_2 Array Efficiencies

For the first experiment the gamma array used was eight BaF_2 modules with photomultiplier tubes, and in the second and third runs, there were 21 modules (plus PM tubes), arranged into three groups of seven. These arrays were situated 'behind' the target, in the backward hemisphere. In each case, each module was instrumented individually, giving eight and 21 channels respectively.

The first array, eight elements of the 42-module, 4π array from Karlsruhe, was protected from the beam pipe by lead shielding, and each module was measured [49] to have an efficiency of 60 % for the 15.11 MeV decay from $^{12}C^*$. This gives a total efficiency (intrinsic + geometrical) of $8/42 \times 60$, or 11.4 %. This figure agrees excellently with Monte Carlo calculations performed using the CERN package GEANT, by Sükösd at Louvain-la-Neuve, giving a figure of 11.5 %.

The array used in the second and third runs, three clusters from the nine-cluster array that is part of the TRASMA apparatus in Catania [50], was calculated to

have an efficiency of 11.4 % for the 15.11 MeV γ-ray; the geometrical efficiency was 14.2 %, and, since this array was used without lead shielding, the intrinsic efficiency for the 15 MeV gamma was larger, at 80 %.

2.3 Detector Configuration

The reaction chamber is illustrated in fig. 2.4. The LEDA sectors were mounted on the inside of the rear door to the chamber, with the pre-amplifiers outside the door. The 16 outputs from each pre-amp box were sent upstairs to the amplifiers and the rest of the electronics. The target was mounted on a wheel, which could be rotated into position, from outside the chamber (thus making it possible to change the target without breaking the vacuum) to align an alpha source (for calibration), an empty target frame, or the target itself, with the beam axis and detectors.

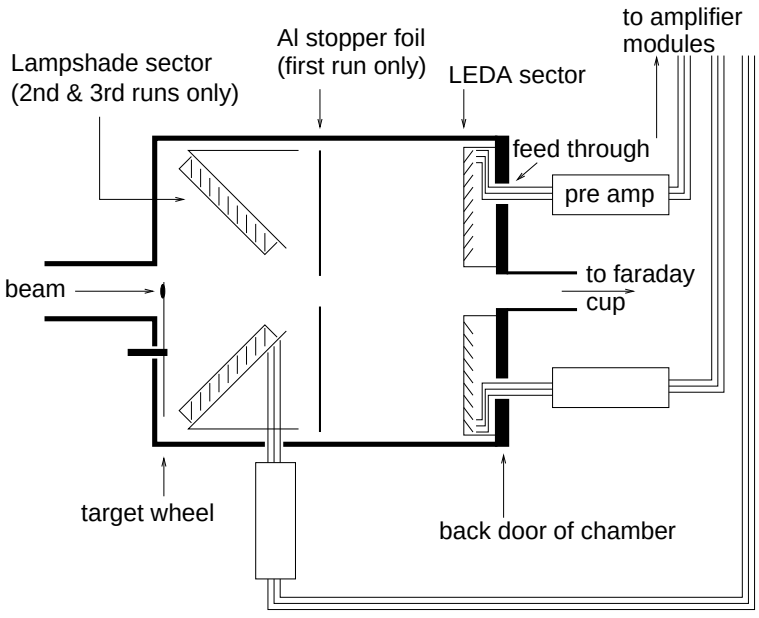

Figure 2.4: *The reaction chamber (not to scale)*

In the first experiment carried out (beam energy 29.5 MeV) one LEDA was used,

with the barium fluoride array. In this case, 20 cm from the target, the silicon covered 15°–32° in the lab frame, with a $\Delta\theta$ for each strip of 1.2°. Each individual strip and BaF_2 module had its own ADC, allowing high multiplicity particle-gamma coincidences to be recorded. There were two TDC channels, one for LEDA and one for the BaF_2 array. An aluminium foil of 11.7 mg/cm^2, sufficient to stop 45 MeV ^{13}N ions, was available to place between the target and LEDA, to prevent heavy ions from reaching the detector. This stopper foil was used for part of the run and the data taken proved to be very instructive, as shall be seen later. A thick aluminium plate was placed in front of the detector to protect it when the beam was being tuned prior to the experimental run.

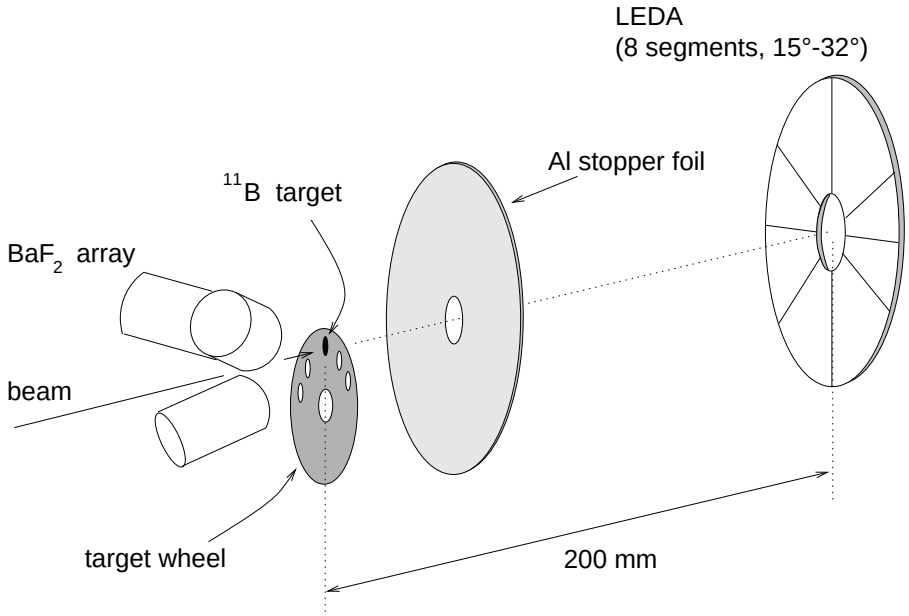

Figure 2.5: *Detector configuration for the 1st run*

In the second and third experiments (at 45 MeV and 29.5 MeV respectively), two LEDAs were used. One was 49 cm from the target, providing coverage from 6°–14°. The second array, dubbed the 'Lampshade,' comprised six segments only, mounted on a flange which was inserted into the reaction chamber. The detector segments that made up this second array were angled forward at 45°, at a distance of 90 mm along the beam axis, to give large solid angle acceptance at more backward

angles, 21°–69°.

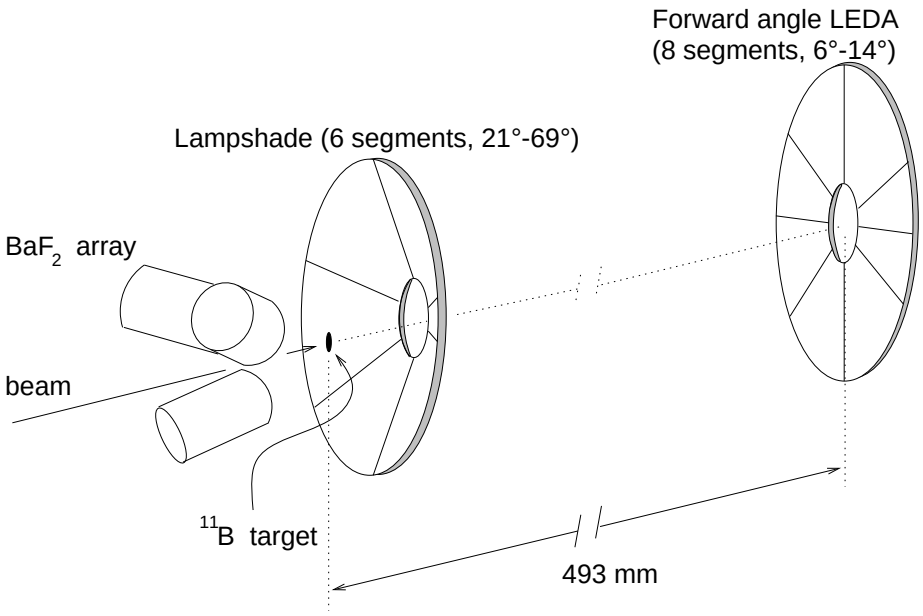

Figure 2.6: *Detector configuration for the 2nd & 3rd runs*

2.4 Data Acquisition

The logic signals and analogue energy signals produced by the the shaping amplifiers were sent to ADC (Analogue to Digital Converter) modules and TDC (Time to Digital Converter) units, powered and controlled by CAMAC crates. The VCC2117/B crate controller buffers the events from the ADCs and TDCs, before sending them block by block to the VME crate, where the acquisition software writes the events to tape and increments on-line spectra; these are stored in RAM in the VME crate and accessed by a PC for viewing (see fig. 2.7).

Each of the detector channels had its own ADC for recording energy signals, and, except for the first run (when there was one TDC for LEDA, and one for the BaF_2 array), its own TDC, in order to measure the time of flight of the reaction products. The ADC modules were 8 channel Silena 4418/V CAMAC ADCs, and

the TDCs were LeCroy 3377 CAMAC TDCs, each supplying 32 channels.

The analogue signals were sent directly to the ADC units. The ECL logic signals were sent to the TDCs, and to the trigger electronics, to generate the ADC gate and determine when the digital energy and time values should be written to tape.

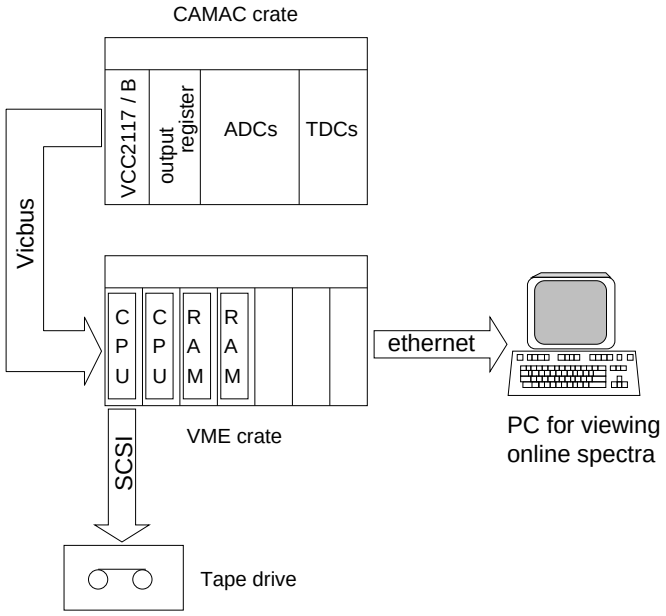

Figure 2.7: *The layout of the data acquisition system*

2.4.1 Trigger Logic

During the first experiment, where one LEDA was used in conjunction with the BaF_2 array, and only two TDC channels were used, the trigger logic was relatively simple. The OR of all LEDA strips was one trigger, and the OR of the BaF_2 modules was the other. With the second and third experiments, however, the situation was complicated by the use of two LEDAs, and of a TDC channel for each individual detector element. The instrumentation no longer fitted into one CAMAC crate, and the extra ADCs and TDCs to be read out and written to tape meant that the acquisition could only operate at around 2 kHz of processed events, as opposed to 10 kHz, and if the trigger logic was kept as it was for the

first run, the dead time would have been unacceptably high, $\sim 50\%$, even with the low current of a radioactive beam. More stringent criteria for the readout of the ADCs were therefore necessary, to reduce the dead time and to ensure that the most interesting events were recorded.

The events of main interest were charged particle hits in coincidence with gamma rays, so again a hit in the BaF_2 array was one trigger. Large numbers of elastically scattered beam particles in the forward angles made it necessary to rate divide the OR of the forward angle LEDA (*ie* one in every n events provided a trigger). The backward angle silicon array, with its large solid angle coverage, saw a large rate of evaporation alphas, and so the OR of these strips was also rate divided, but by a lesser amount. There was no multiplicity requirement on the rate-dividers. This meant that high multiplicity events contained solely within LEDA or within the Lampshade would also be rate-divided as well as the multiplicity one elastic scattering events, but since the individual triggers were ORed together, if there was a LEDA-Lampshade coincidence or a detected gamma photon then the whole event (*ie* all ADC and TDC hits) would always be written to tape, regardless of the rate dividing on the LEDA OR. An indication of dead time was obtained by recording the total number of triggers arriving at the latch, and also the rate at which the latch actually fired, *ie* the rate of accepted triggers.

The logic applied to each of the sets of detectors (forward angle LEDA, Lampshade and BaF_2 modules) is illustrated in figures 2.9, 2.10 and 2.11. At several points in the circuit, rates such as the rate of events in LEDA, accepted triggers *etc*, were recorded in CAMAC scaler modules, for writing to tape, and were also sent to digital display modules to allow online visual inspection. The triggers from each set of detectors are brought together in an OR gate before being ORed with the high frequency (HF) signal from the cyclotron. This provided a timing baseline for the TDCs. The analogue HF signal had first to be turned into logic pulses before it could be included in the trigger electronics; this was done by applying a leading-edge discriminator.

Figure 2.8 shows the relationship between the HF signal, the pulse train derived from it, and an detector event associated with a reaction induced by the beam (as opposed to a background event). The trigger from the detectors starts the TDC, which is then stopped by the *next* HF pulse. The value produced by the TDC is therefore shorter for a longer time of flight, because the longer the time of flight, the sooner the next HF pulse arrives after the detector event. The time of flight is therefore some constant minus the TDC value. The constant will be related to the beam pulse period, with other factors caused by the timing and delays in the trigger electronics.

To record a measurement of the beam current, which fluctuated somewhat during the runs, a faraday cup at the end of the beam line was used with an Ortec 439 current digitiser, the output from which was passed to a CAMAC scalar module to record the number of pulses onto Exabyte tape along with the ADC and TDC data. The total count recorded in the scalers in a particular length of time is proportional to the charge received by the digitiser and therefore to the beam current during that interval. The DC offset in the cup was measured by recording scalers during a period of time when the beam was off.

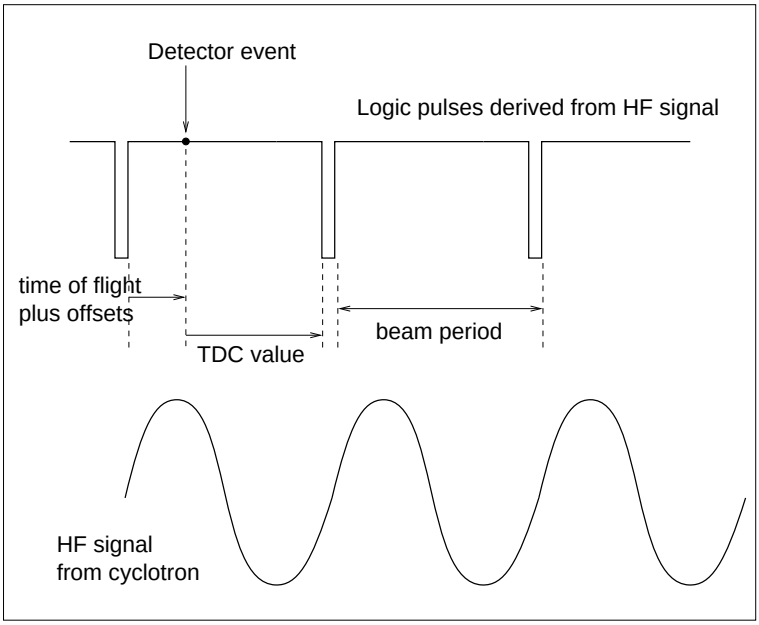

Figure 2.8: *Time of flight and TDC value*

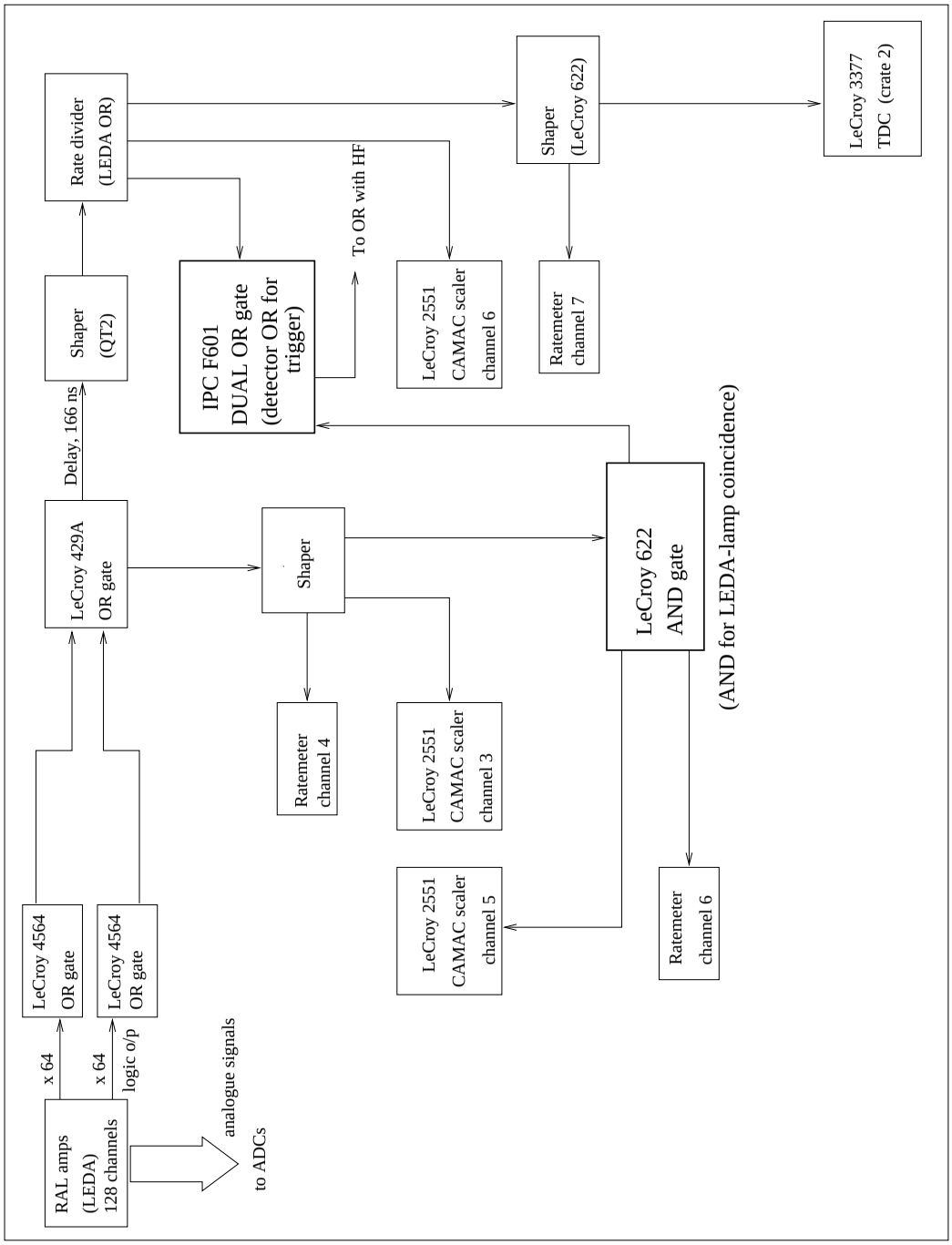

Figure 2.9: *LEDA trigger logic*

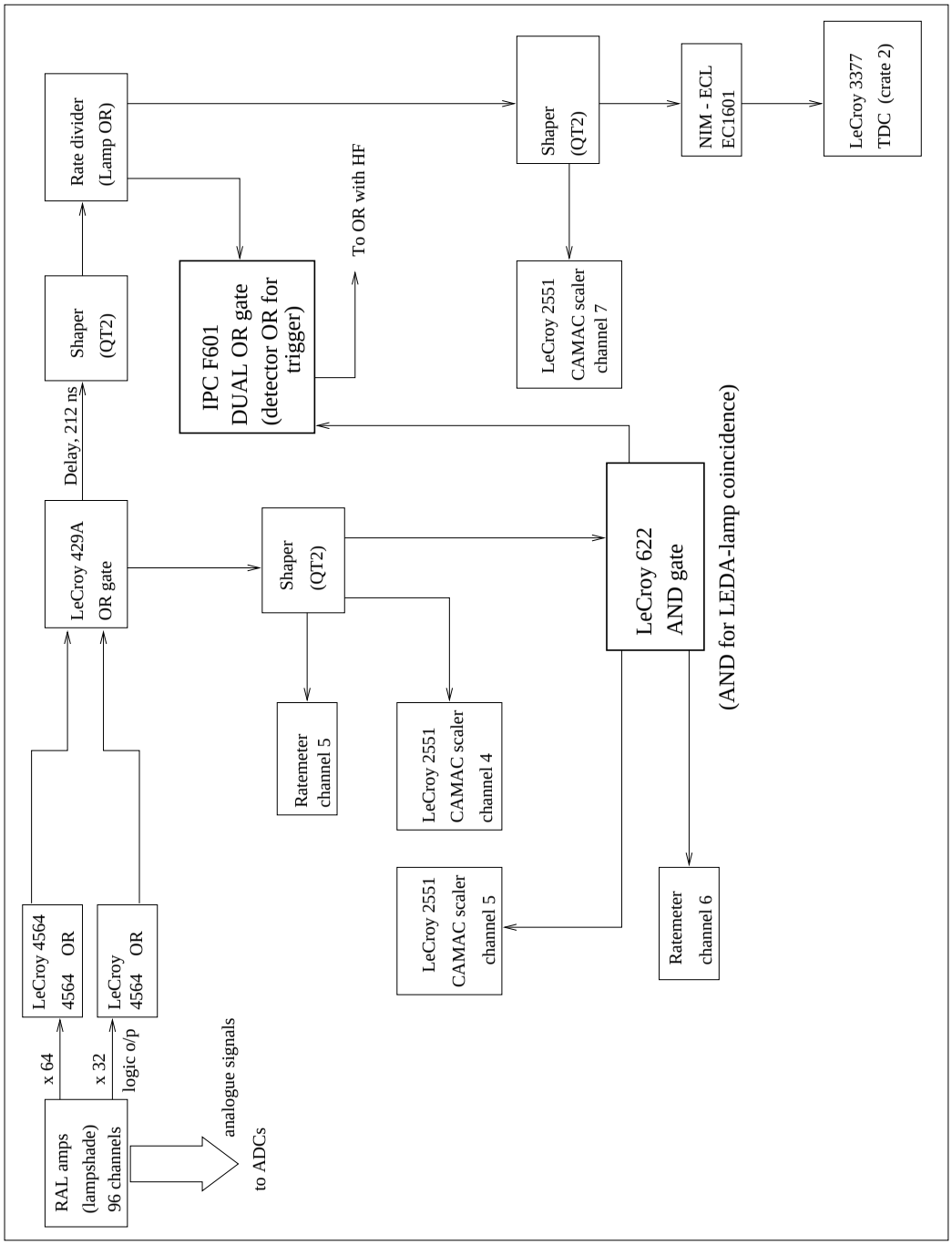

Figure 2.10: *Lampshade trigger logic*

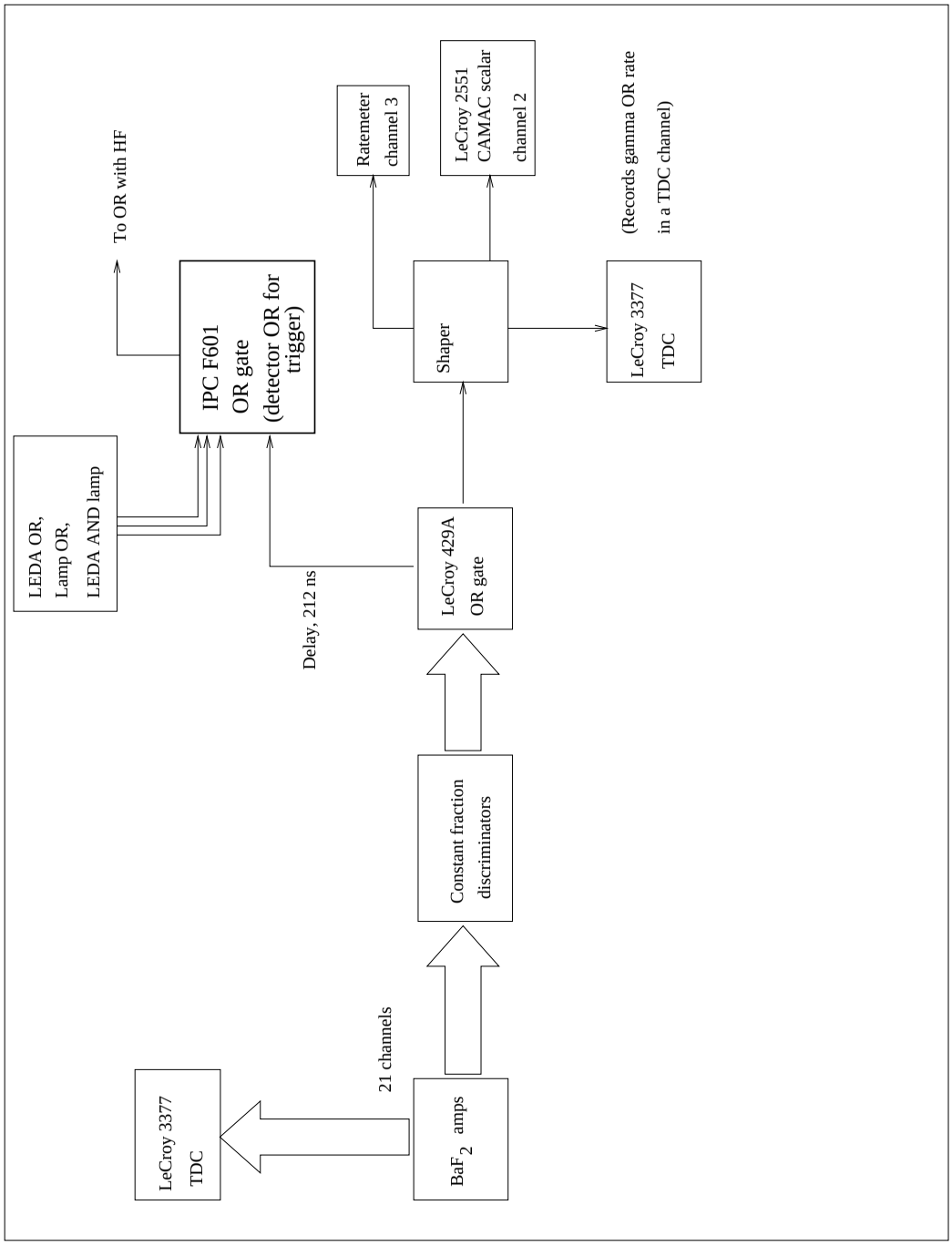

Figure 2.11: *BaF_2 trigger logic*

Chapter 3

Experimental Data

This chapter shall describe how the experimental data, once obtained and recorded on tape, was extracted and analysed.

3.1 Extracting Data From Tape

The data recorded on digital tape was subsequently extracted and analysed with `sort-shell` [51], a program which sorts event-by-event data and processes it with a linked module written by the user, allowing generation of spectra following user-defined criterion of, for example, coincidence requirements, energy gates *etc.* `sort-shell` reads events from tape or disc and returns the number of ADC and TDC hits in that event, and the ADC and TDC contents for each hit. An example of a user-written sort module in FORTRAN is shown in fig. 3.1. This example generates LEDA spectra, numbered by strip number 0–127, a hit pattern (spectrum #256) and a multiplicity spectrum (#512), discarding the high multiplicity pulser events. Timing criteria can be introduced by referring to the TDC hits, which are indexed by numbers 256–511.

```
subroutine uevent(trig,noadcs,adcs,convs)
     if(noadcs.gt.30) goto 999      Escape if there are more than 30 ADC
                                    and TDC hits in the event; it's probably
                                    a pulser event.

     do 200 i=0,noadcs-1            Loop through the ADC/TDC hits.
        n=adcs(i)                   adcs(i) is the index number of the (i+1)th hit ...
        if(n.lt.128) then           ... those below 128 represent LEDA ADC hits
           mleda=mleda+1            Generate the LEDA multiplicity for the event.
           call rinc(n,convs(i))    Increment the n^th spectrum with the
                                    ADC value for this hit
           call rinc(256,leda)      Increment a hit pattern spectrum for LEDA.
        endif
200  continue
     call rinc(512,mleda)           Increment a multiplicity spectrum for LEDA.
999  continue
     return
```

Figure 3.1: *A sample* `sort-shell` *sort module*

3.2 Detector Geometry

In order to calculate relative and absolute cross sections for the reaction being studied, it is necessary to know the position and solid angle of each detector element. This is not as trivial a calculation as might be thought, due to the complex nature of the detector configuration.

3.2.1 Calculation of Solid Angles

For the eight segment forward angle LEDA detector calculation of the solid angle subtended by each strip is straightforward—each strip is annular (see fig. 3.2),

and the integration

$$\omega = \iint \sin\theta \; d\theta \; d\phi$$

is carried out with θ and ϕ independent of each other, so for a given strip in LEDA,

$$\omega = \Delta\phi \left[\cos\theta_{min} - \cos\theta_{max}\right]$$

The results of this calculation for LEDA at 200 mm from the target (as in the first experimental run) and at 493 mm (second and third runs) are shown in table 3.1.

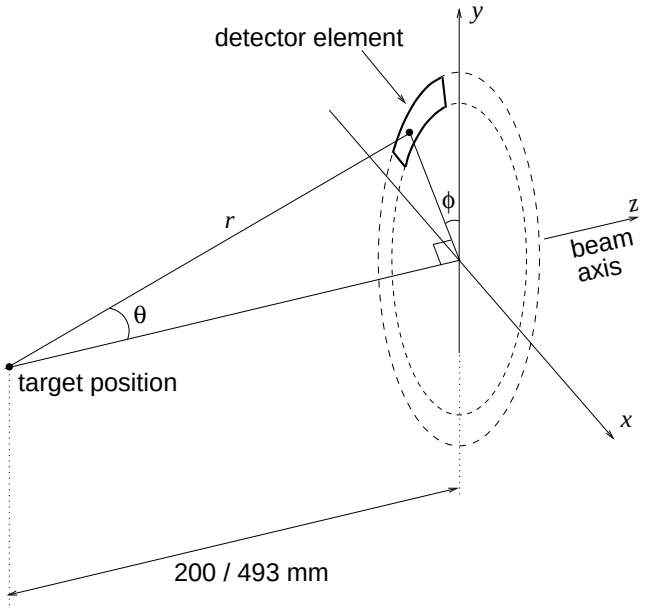

$$x = r \sin\theta \sin\phi$$
$$y = r \sin\theta \cos\phi$$
$$z = r \cos\theta$$

Figure 3.2: *LEDA solid angle geometry*

For the Lampshade detector array, the calculation is complicated by the fact that the strips are inclined at 45° to the target and are therefore no longer annular—the geometry is very difficult to calculate analytically. The solid angle has therefore been determined by a Monte Carlo approach, by which hypothetical particles

strip #	θ_1	ω_1 (sr)	$\theta_{2,3}$	$\omega_{2,3}$ (sr)
0	32.5^o	3.20×10^{-3}	14.5^o	7.96×10^{-4}
1	31.5^o	4.81×10^{-3}	13.9^o	1.19×10^{-3}
2	30.4^o	6.09×10^{-3}	13.4^o	1.43×10^{-3}
3	29.4^o	6.97×10^{-3}	12.8^o	1.62×10^{-3}
4	28.3^o	6.93×10^{-3}	12.3^o	1.55×10^{-3}
5	27.1^o	6.74×10^{-3}	11.7^o	1.50×10^{-3}
6	25.9^o	6.66×10^{-3}	11.2^o	1.42×10^{-3}
7	24.8^o	6.47×10^{-3}	10.6^o	1.35×10^{-3}
8	23.6^o	6.32×10^{-3}	10.1^o	1.28×10^{-3}
9	22.4^o	6.23×10^{-3}	9.5^o	1.21×10^{-3}
10	21.2^o	5.90×10^{-3}	8.9^o	1.17×10^{-3}
11	19.9^o	5.66×10^{-3}	8.4^o	1.08×10^{-3}
12	18.6^o	5.41×10^{-3}	7.8^o	1.01×10^{-3}
13	17.4^o	5.09×10^{-3}	7.2^o	9.40×10^{-4}
14	16.0^o	4.78×10^{-3}	6.6^o	8.57×10^{-4}
15	14.7^o	4.45×10^{-3}	6.1^o	7.93×10^{-4}

Table 3.1: *Geometry of one LEDA sector in the first run* (θ_1, ω_1) *and the second & third runs* $(\theta_{2,3}, \omega_{2,3})$

originating from the target, isotropically and with random θ and ϕ, are tracked to see whether or not they intersect the detector. The fraction of the total number of particles incident on each strip gives the solid angle as a fraction of 4π (or rather, of $\pi/4$, since the events were restricted to $0 \leq \theta \leq \pi/2$, $0 \leq \phi \leq \pi/4$ for reasons of efficiency; a whole segment sits well within this cone and there is no need to simulate particles outside it).

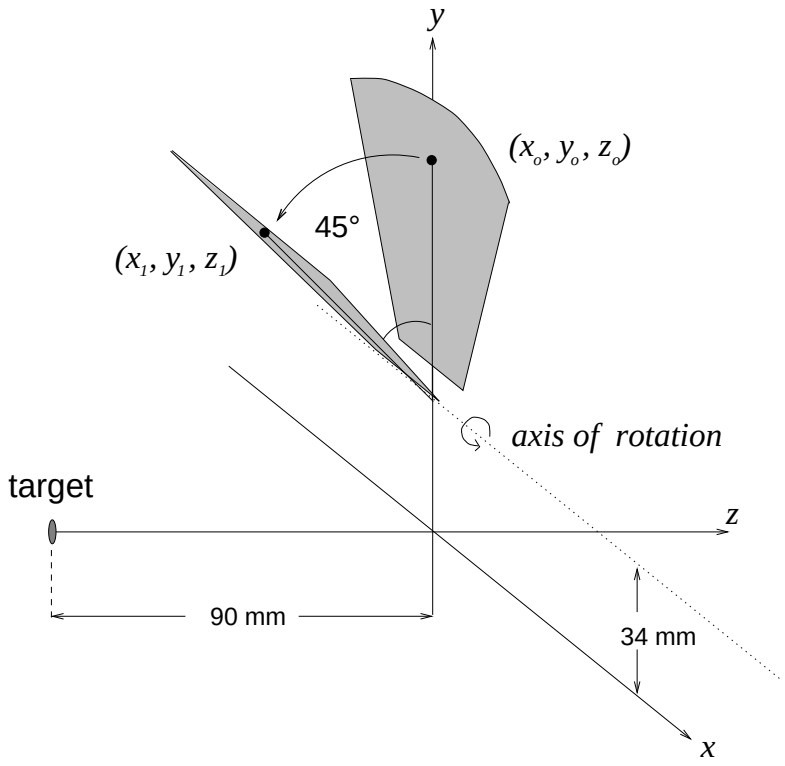

Figure 3.3: *Rotation of a LEDA segment into the Lampshade configuration*

To determine whether a particle at a given θ and ϕ hits the detector, a single segment of the array is considered in its usual position, normal to the beam axis. The set of points (θ_0, ϕ_0, r_0), or (x_0, y_0, z_0) on the detector are rotated through 45° in the yz plane to give their positions (θ_1, ϕ_1, r_1) in the Lampshade array (see fig. 3.3). The test particles are then tracked from the origin to see whether they intersect the set of points (θ_1, ϕ_1, r_1), *ie* whether they hit the detector. The same method without the rotation reproduces the solid angle of the plane LEDA. This approach is easily modified to include the effects of an extended source diameter

strip #	θ_{lab}	ω (sr)	strip #	θ_{lab}	ω (sr)
0	67.3°	1.71×10^{-2}	8	42.9°	3.56×10^{-2}
1	64.5°	3.00×10^{-2}	9	39.7°	3.28×10^{-2}
2	61.6°	3.82×10^{-2}	10	36.6°	3.06×10^{-2}
3	58.6°	4.03×10^{-2}	11	33.5°	2.81×10^{-2}
4	55.6°	4.01×10^{-2}	12	30.4°	2.54×10^{-2}
5	52.4°	3.96×10^{-2}	13	27.5°	2.25×10^{-2}
6	49.3°	3.85×10^{-2}	14	24.6°	1.98×10^{-2}
7	46.1°	3.72×10^{-2}	15	21.9°	1.77×10^{-2}

Table 3.2: *Solid angle of one Lampshade sector*

(for the alpha calibration runs) or beam spot size (for the experiment proper); the trajectory of the particle is offset by a random amount Δx and Δy.

The effective solid angle subtended by a 2 mm beam spot (as measured from the burn mark inscribed on the target by the beam), with a square beam profile, was calculated, and differs from that for a point source by no more than 3% for any strip in the Lampshade array; for the plane array, 200 mm or 493 mm from the target, the effect is negligible.

3.2.2 Angular Position of the Strips

The values of θ shown in tables 3.1 and 3.2 are simply the central values for each strip, $\theta_c = \theta_{min} + \Delta\theta/2$. However, it has been shown by Lafferty and Wyatt [52] that data points in large bins (which the counts measured in the Lampshade detector elements certainly are) should not necessarily be represented by $f(\theta)$ at θ_c, but that in fact it depends on the distribution being measured. For example, if the real distribution rises sharply across the width of the bin, the measured value of $f(\theta)$ will be weighted towards a larger value of θ than θ_c. The choosing of the

"average" value of θ is further complicated here by the unusual detector geometry. In view of this, and taking into account the distributions being measured and the theoretical predictions they are to be compared with, the values of θ at which the data points are placed shall be reconsidered later.

3.3 Energy Calibration

With over 200 individually instrumented detection channels, it is necessary to gainmatch the energy scales—individual pre-amps and amplifiers will have slightly different gains and offsets. The energy scales need to matched with each other because, under the conditions of low statistics associated with a radioactive beam, the output from each detector element will need to be summed together. This gainmatching was most conveniently carried out offline, using data from calibration runs.

3.3.1 LEDA Calibration

For the silicon detectors the calibration was carried out by using a mixed ^{239}Pu-^{241}Am-^{244}Cm alpha source which was rotated into the target position on the target wheel; the beam was turned off and data was taken to tape as usual, except that the HF dependence was removed from the trigger and the rate-dividing was turned off, because the source was obviously not correlated with the cyclotron, and the count rate with the alpha source was low. Fig 3.4 shows a typical alpha calibration spectrum.

The energies assumed for the α peaks were corrected for the energy loss in the dead layer; at 25°, a 5.486 MeV α will lose 60 keV in a 0.3 μm dead layer of aluminium, a 1% effect, leaving it with 5.426 MeV. The effect of energy loss in the dead layer also needs to be considered in the experimental data proper—

for 20 MeV ^{13}N or ^{12}C the effect is of the order of 1 MeV—however, it is not appropriate to apply such a correction indiscriminately because, of course, the experimental spectra contain a range of different particles for which aluminium will have widely differing stopping power.

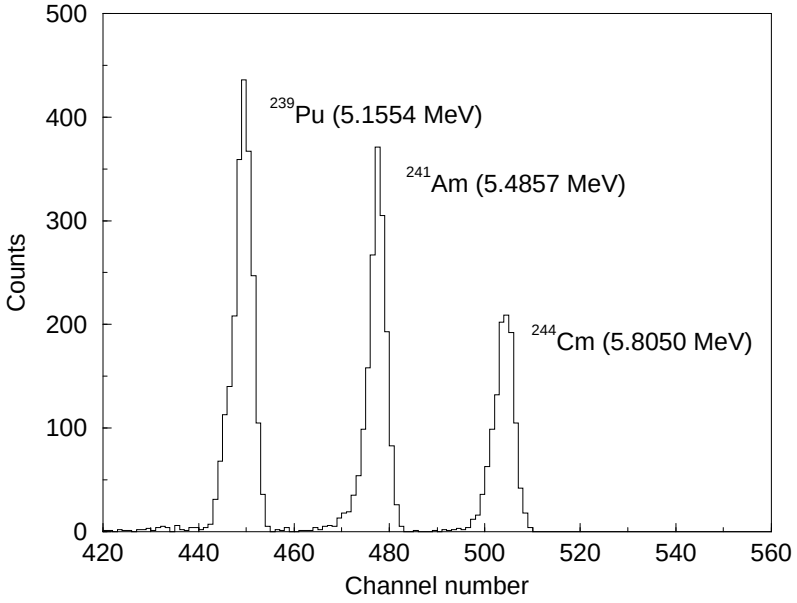

Figure 3.4: *Alpha calibration spectrum*

However, the positions of the source lines only gives an indication of the relative gains of each detector-pre-amp-amplifier channel. To measure the electronic offset, a BNC pulse generator was used to feed a series of pulses into the LEDA pre-amps, with regularly spaced pulse heights. This pulser walkthrough also gives an indication of the linearity of the ADC—the non-linearity was found to be less than 1%. The pulser was left running at a fixed setting, at about 1 Hz, throughout the experimental run, to give an indication of any possible gain shifts—pulser events were easily removed from the analysed data by sorting with a multiplicity condition, as in the `sort-shell` sort-module shown in fig. 3.1

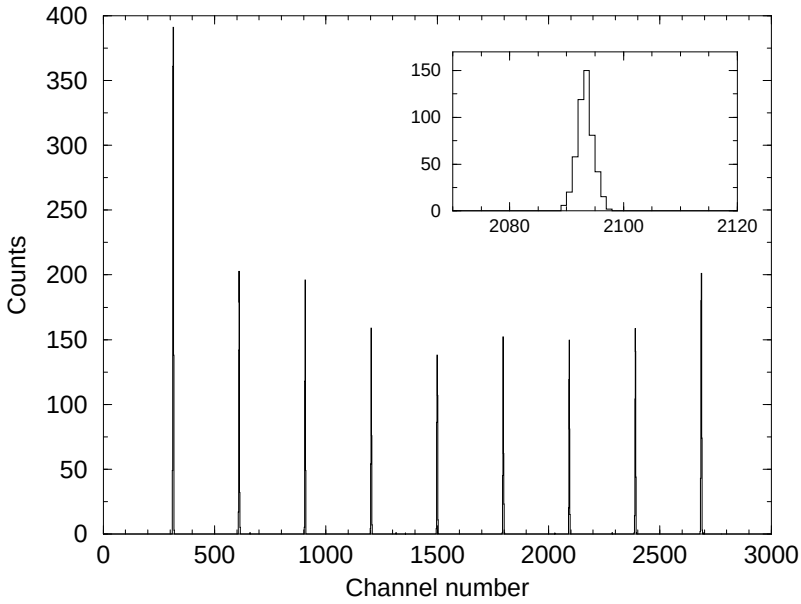

Figure 3.5: *A typical pulser walkthrough spectrum*

Energy resolution

The pulser spectrum gives a measure of the electronic noise; in this case, the fwhm of the peaks is around 4 channels, corresponding to 52 keV. The alpha spectra (fig. 3.4) showed a width of typically 60 keV. The straggling of the alphas in the aluminium window on LEDA is expected to be given by $\delta E = 25\sqrt{\Delta x}$ keV [53], where Δx is the thickness of the dead layer in microns. This gives 25 keV for a 1 μm aluminium window. Combining the electronic noise with this straggling factor to give the expected experimental resolution σ, with

$$\sigma = \sqrt{\sigma_e^2 + (\delta E)^2} \tag{3.1}$$

we obtain 61 keV, in reasonable agreement with the resolution achieved with the alpha source.

3.3.2 BaF_2 Energy Calibration

In the case of the barium fluorides, a beryllium-alpha neutron source was used. This was a combined ^{9}Be and ^{241}Am source, giving the reaction $^{9}\mathrm{Be}(\alpha,\mathrm{n})^{12}\mathrm{C}^{*}$. Apart from neutrons, this source produces gamma rays at 4.44 MeV, a transition from $^{12}\mathrm{C}^{*}$, which were used to calibrate the detectors. Figure 3.6 shows a calibration spectrum from one BaF_2 module taken with the αBe source. For $E_\gamma = 4.44$ MeV, the first escape peak should be at 3.93 MeV and the energy of the Compton Edge, should be 4.32 MeV, as given by

$$E_{compton} = \frac{2E_\gamma^2}{m_e c^2 + 2E_\gamma} \tag{3.2}$$

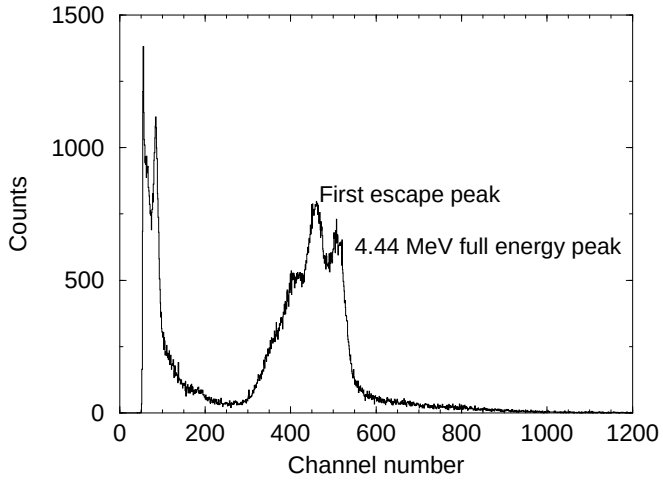

Figure 3.6: *A typical BaF_2 calibration spectrum*

The second calibration point for the gamma detectors was the 15 MeV peak (from $^{12}\mathrm{C}^{*}$) in the experimental data.

With arrays of eight (first run) or 21 (second and third runs) individual crystals, it is in principal possible to reconstruct events where a photon escapes from the crystal, or is Compton-scattered out of the crystal, before it deposits its full energy.

By adding up the energies observed in neighbouring modules, the full energy could be measured. However, in these experiments, with the attendant high background rates, a threshold of around 4 MeV was used. This makes reconstruction of the full energy impossible for most gamma photons since the energy deposited in a neighbouring crystal by a Compton scattered or escape photon would be rather likely to be below threshold. For the purposes of this analysis, therefore, each crystal was considered separately. This results in a diminished efficiency for the array, compared to that of one large module, but not to the extent that too many interesting events are lost.

3.4 Normalising Cross Sections

It is obviously desirable to obtain absolute differential cross sections for the transfer reaction, rather than relative cross sections which can only be compared with each other. Rutherford scattering proved not to be a reliable source of a scaling factor for obtaining absolute cross sections, because most of the data was taken at angles above the grazing angle; θ_g at 29.5 MeV (45 MeV) is 18° (11°). The data available with $\theta_{lab} < \theta_g$ could not be used because of contaminants, including oxygen, in the boron target, in unknown quantities. It shall be seen in the experimental results shown below that elastic scattering from these contaminants and from ^{11}B could not be resolved in the LEDA spectra—see the spectra below.

In order to calculate the absolute differential cross sections, we need

- the solid angle subtended by each detector element, as described on page 32;
- the total beam incident on the target, and
- the thickness of the target.

3.4.1 Beam Current

The beam current was calculated by means of the scalers recorded on tape from the faraday cup/current digitiser. Summing these scalers gives a measure of the integrated charge at the faraday cup, and hence the beam current. The dead time of the acquisition is measured by counting the total triggers and the accepted triggers, also recorded on tape. The faraday cup amplifier had a gain of $\times 1000$, and the current digitiser was set to generate one pulse per 10^{-10} C of charge, so the total charge incident on the faraday cup is given by

$$Q = \frac{N_{pulse} \times 10^{-10} - I_0 t}{1000} \tag{3.3}$$

... where N_{pulse} is the number of pulses in a given time interval t and I_0 is the DC offset from the faraday cup. If the beam is in charge state q when it reaches the faraday cup, the number of particles incident on the target is given by

$$N_p = \frac{1}{q}\left(\frac{N_{pulse} \times 10^{-10} - I_0 t}{1000}\right) \tag{3.4}$$

... assuming that the beam is negligibly attenuated in the target.

The initial charge state of the beam is 2^+ or 3^+, depending on the beam energy. However, in passing through the target the beam reaches an equilibrium charge state q. This has been calculated using the local code `csd`, which follows the method of Dmitriev & Nikolaev [54], giving $6.5e$ at 29.5 MeV and $6.8e$ for 45 MeV.

However, the dead time of the acquisition must also be taken into account; for this purpose the total number of triggers N_{trigg} and the number of accepted triggers $N_{accepted}$ were recorded on tape. To calculate the cross sections we can use a quantity Q_{eff}, the effective charge incident on the cup, which is the total charge scaled by the accepted triggers as a fraction of the total triggers, *ie* scaled by the live time. This is necessary because beam incident on the target and the reaction

products incident on the detectors while the acquisition is dead are effectively lost.

Because the values N_{pulse}, N_{trigg} and $N_{accepted}$ were recorded each time a block of data was written to tape, it is convenient to calculate the effective charge as

$$Q_{eff} = \sum \frac{1}{1000} \left(N_{pulse} \times 10^{-10} - I_0 t \right) \times \frac{N_{accepted}}{N_{trigg}} \tag{3.5}$$

and if a particular strip with solid angle ω gives a yield of events Y, the differential cross section will be given by

$$\frac{d\sigma}{d\Omega} = \frac{q}{Q_{eff} N_t \epsilon_\gamma} \frac{Y}{\omega} \tag{3.6}$$

N_t is the number of target nuclei per unit area, given by the target thickness.

The factor of ϵ_γ, the efficiency of the BaF_2 array, appears because we are interested here in gamma-particle coincidences. This value must incorporate the geometrical efficiency of the BaF_2 array, the response of the array to γ-photons with a full energy of 15.11 MeV, and also the probability that the 15.11 MeV state in ^{12}C will gamma decay all the way to the ground state, rather than to another excited state or *via* α-decay. The widths Γ_α and Γ_γ for α- and γ-decay are 1.8 eV and 41.8 eV respectively, and the total branching ratio for γ-decay to the ground state is 73% [55].

3.4.2 Target Thickness

The target thickness was measured by observing the energy loss suffered by ^{241}Am α particles (5486 keV) as they passed through the target. The measured ΔE, 540 keV, was translated into a thickness by considering the stopping power of ^{11}B, as given by the local code `dedx`, which is based on the Oak Ridge `spar` code [56]. The measured thickness was 800 $\pm$ 100 $\mu g\,cm^{-2}$, giving an areal density of ^{11}B nuclei N_t=4.2×10^{19} cm^{-2}.

The measurements of beam current and target thickness introduce a systematic error of ± 20% to the absolute cross sections, in addition to the statistical errors.

3.5 Experimental Results

3.5.1 First Run: 29.5 MeV

The first experiment, performed in march 1994 with a beam energy of 29.5 MeV, gave the first evidence of the transfer reaction. An average of 12 ppA of beam was achieved for 15 hours, giving a total of 4×10^{12} particles on the target. The target was 800 $\mu g\,cm^{-2}$ of 95% enriched ^{11}B.

LEDA spectra

LEDA singles spectra show the elastic scattering of the beam (fig. 3.7). At 32°, peak A in fig. 3.7 at $\sim$ 16 MeV is the elastic scattering of ^{13}N from ^{11}B; however it shows other structure; we would not expect either the recoil ^{11}B or scattering off the 5% of ^{10}B to be fully resolved. Peak B at 18 MeV is at the expected energy for $^{16}O(^{13}N,^{13}N)$, but again, it shows unresolved structure. There are also clearly at least two unresolved peaks at 23 MeV (C in fig. 3.7)—this feature does not move as the angle varies, and so is probably associated with a heavy contaminant, possibly tantalum.

Looking at the two-dimensional spectrum for the same events, plotting TDC value against ADC, we see that, for the 15 MeV peak at least, the situation can be improved a little. Note that the time axis is the reverse of the time of flight, for reasons explained in Chapter 2. The main features are a two branches of events differing in time of flight. The upper branch, *ie* the events with the *shorter* time of flight are alpha particles—for a given energy, their shorter time of flight means

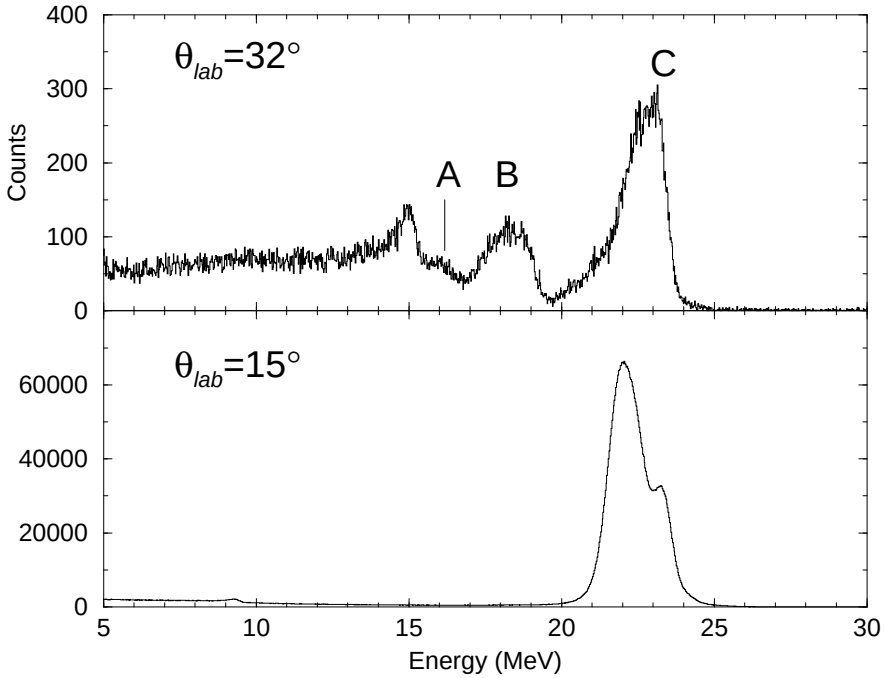

Figure 3.7: *LEDA singles spectra*

they must be of smaller mass than the lower branch, of heavy ions. In the data taken with the aluminium stopper foil, which prevented heavy ions such as ^{12}C and scattered beam particles from reaching LEDA, but allowed α's and protons through, this branch of heavy ions does not appear. Also seen in this spectrum are the βs and protons, which punch through the silicon at lower energies than the α particles.

The tape sorting program `sort-shell` allows the user to place a polygon window around any region of a 2-D plot and sort events with the condition that they be inside or outside that window. By putting a window around the branch of heavy ions in fig. 3.8, and projecting onto the energy axis, we can exclude the branch of alpha particles which intrudes into the same energy region as the ostensible elastic scattering events (fig. 3.9). The resulting spectrum is a little cleaner—the peak at 15 MeV at 32° turns out to be alpha particles and a peak at 16 MeV becomes slightly more obvious, but, as is plain from the 2-D plot, the events that overlap

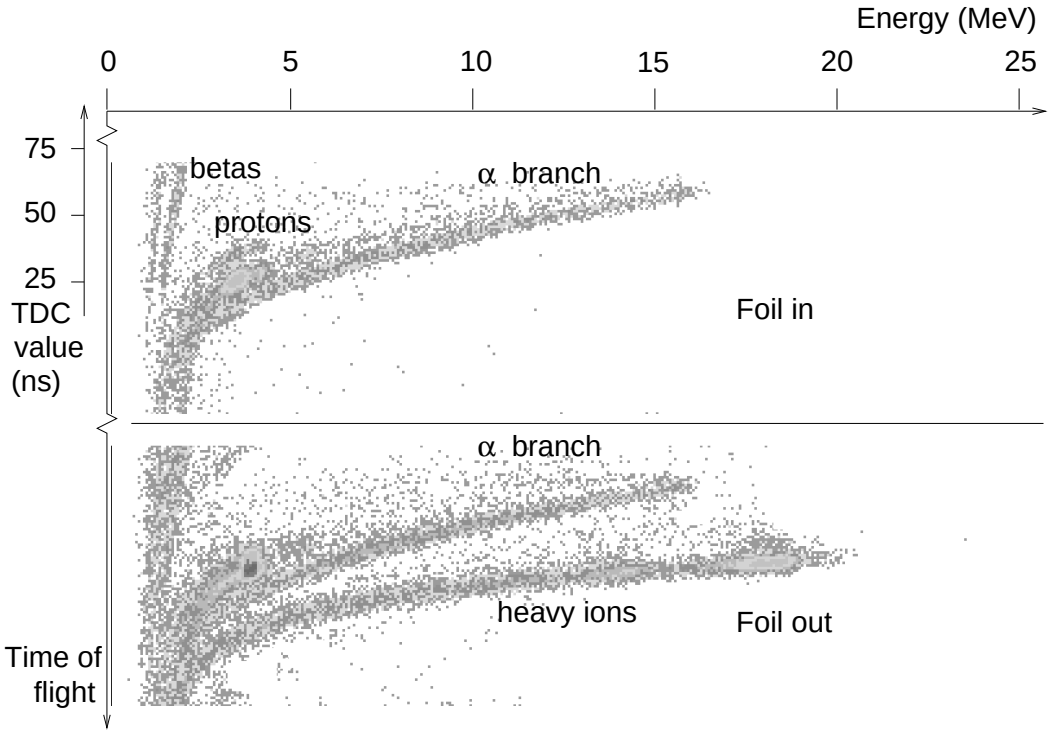

Figure 3.8: *2-D LEDA singles spectra, 32°, taken with the stopper foil (upper plot) and without (lower plot)*

the region of interest for ^{13}N elastic scattering are other heavy ions and cannot be gated out by virtue of their time of flight.

At 15°, below the grazing angle, where we might wish to use the elastic scattering to normalise for absolute cross sections, the peaks seen at 32° have merged together (as we would expect from the kinematics). If we assumed that this large peak was only due to ^{11}B(^{13}N,^{13}N), our normalisation factor for the cross sections would be over-estimated, due to the contribution from other scattering centres.

Gamma spectra

Turning to the γ spectra, we see the 15 MeV ^{12}C* peak, and a large continuum of events at higher energies (fig. 3.10). In the hostile (in the context of taking nuclear reaction data) environment of a radioactive beam, we might expect a strong

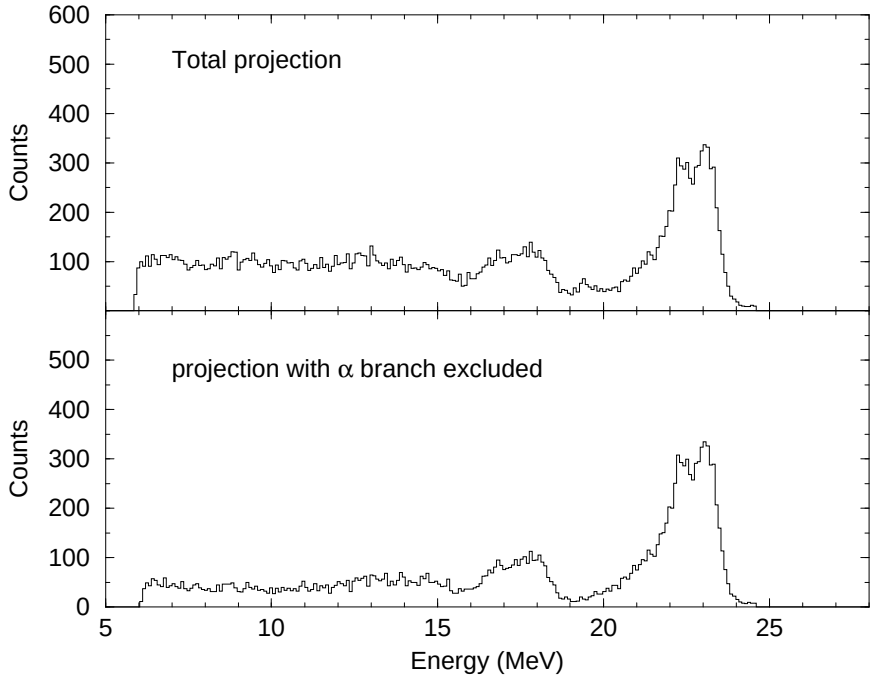

Figure 3.9: *Projections of 2-D LEDA spectrum in fig. 3.8*

background of unwanted events. Fortunately, a large amount of this background can be removed, by referring to the TDC values associated with the gammas.

The Common Stop input to the TDC module is taken from the HF signal from the cyclotron, giving a timing reference point. This gives a sharp peak in the TDC spectrum (fig. 3.11), corresponding to γ events in coincidence with a beam pulse.

Two peaks appear in fact because only every second beam pulse was used in the Common Stop input of the TDC module. This was done to allow examination of the rate of randomly coincident events from consecutive beam pulses. It also shows that, in this case, the beam period was 92 ns. Gating on these peaks reduces the background in the gamma spectrum, and in the LEDA spectra in the case of γ-particle coincidences.

There will of course be background events in random coincidence with a beam

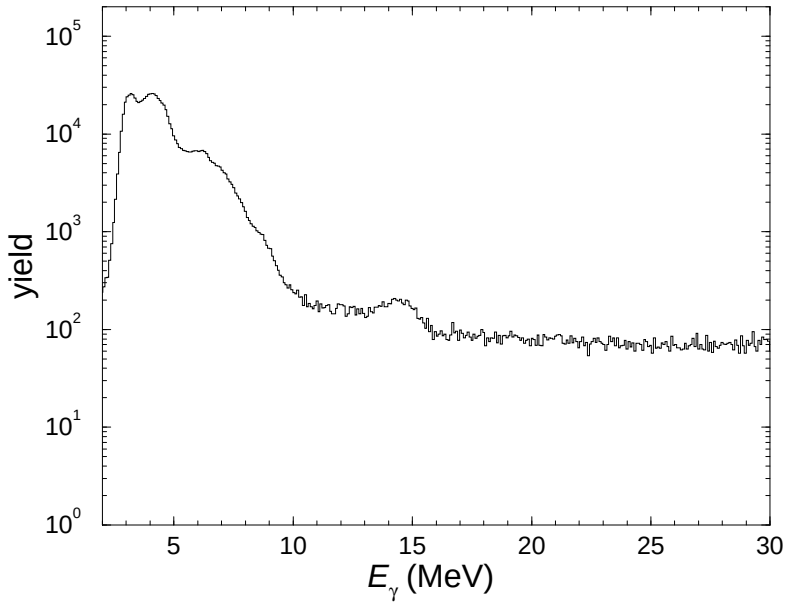

Figure 3.10: *Ungated BaF_2 γ spectrum*

pulse; these can be removed by gating away from the TDC peaks, on the background continuum (keeping the time gate the same width), to generate a spectrum of background events (see fig. 3.12). Subtracting this background gives a much cleaner spectrum (fig. 3.13), with almost no counts at higher energies than the peak at 15 MeV.

That peak persists in the spectra gated on a hit in LEDA. However, for the data taken with the aluminium stopper foil, this peak disappears from the gamma-particle coincidence spectrum (fig 3.14). This tells us that the 15 MeV peak is associated with a heavy ion, which is stopped in the foil before it reaches LEDA.

Particle-gamma coincidence spectra

LEDA spectra gated on the 15 MeV peak show two very distinct peaks, with almost no background. Figure 3.15 shows a typical LEDA spectrum with this

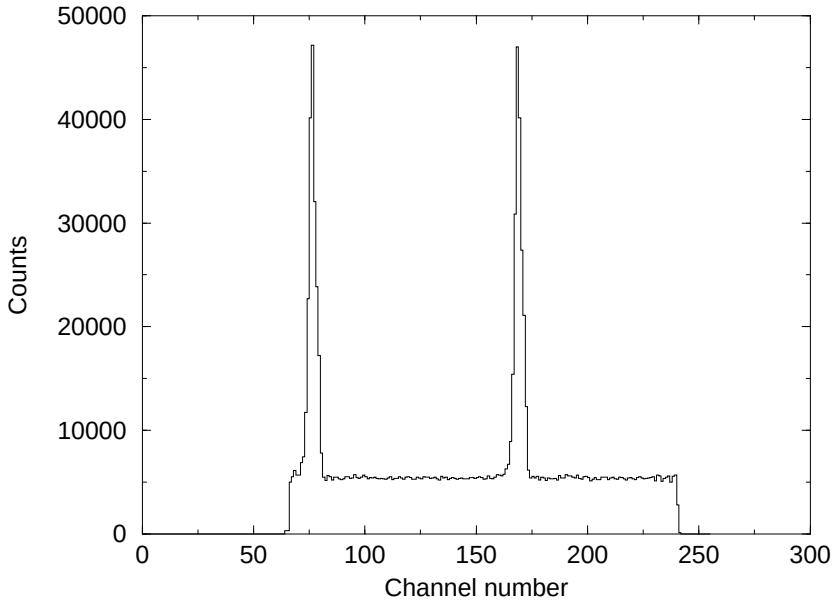

Figure 3.11: *A typical BaF_2 TDC spectrum*

gating; this is the sum of the response for all eight strips at a given radius in the array. These peaks are much stronger at forward angles, and their positions have a very clear angular dependence. This angular dependence agrees very strongly with the kinematics of ^{11}B(^{13}N,^{12}C*)^{12}C*, with one carbon in the T=1, J^π=1$^+$ 15.11 MeV state, and the other in either the T=0, J^π=0$^+$ ground state or the first excited state at 4.44 MeV, T=0, J^π=2$^+$. Figure 3.16 shows the comparison between a two body kinematics calculation for the reaction and the observed peak positions. The data here have been corrected for the expected energy loss in the dead layer (about 1 MeV). It is possible, however, that the thickness of the aluminium contact varies across the detector, so a certain departure from the theoretical curve is to be expected. The error bars reflect this, and a dead thickness of 1 $\pm$ 0.5 μm has been assumed. There is also the possibility of radiation damage causing dead volumes in the detector which cause incomplete charge collection and which might not be uniform across the different strips. However, the agreement here is rather good. In principle, it could also be possible to see the 4.44 MeV

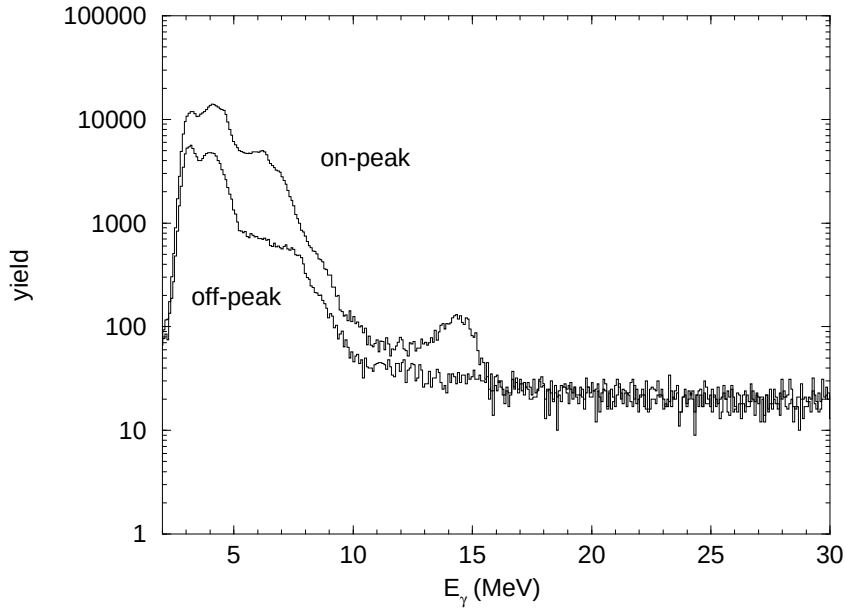

Figure 3.12: *Gamma background subtraction*
Spectra gated on and off TDC peaks

gamma from the de-excitation of the 2^+ ^{12}C product that remains from those transfer events associated with the lower energy peak in figure 3.15. However, the efficiency of detecting both γ-photons would be of the order of ϵ_γ^2, $\sim$1%, and the statistics obtained would be very poor.

The kinematics and the coincidence with the 15 MeV transition lead us to conclude that the transfer reaction is being observed. Unfortunately, the opening angle of the two carbons in the lab frame is larger than the detector geometry (see Appendix A), so carbon-carbon coincidences could not be measured.

3.5.2 Experiments 2 and 3

For the second and third runs the two silicon arrays were used in the LEDA-Lampshade configuration. In the second experiment the beam was $^{13}N^{3+}$ beam

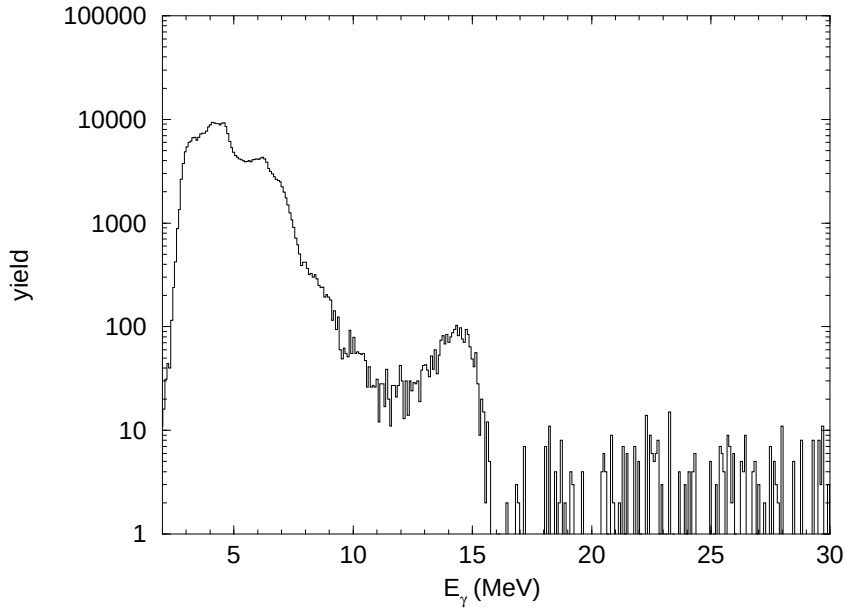

Figure 3.13: *Background subtracted gamma spectrum*

at 45 MeV, and an average of 2.1 ppA was achieved for 52 hours, giving a total of 2.5×10^{12} particles on the target. For the third run we returned to the lower energy $^{13}N^{2+}$ beam at 29.5 MeV, repeating the first experiment at more forward and more backward angles. The beam ran at 12 ppA for 69 hours, a total of 1.8×10^{13} particles incident on the target.

The data from these runs was analysed using the same methods as for the first experiment, as described above. The signature of the transfer reaction was again observed when gating on the 15 MeV gamma transition. The cross section falls off rapidly at backward angles, and in the Lampshade the transfer reaction was only measurable for a few of the innermost strips.

The measurement of the cross section of the transfer reaction was slightly complicated here because, with the use of two silicon arrays, there was the possibility of observing both carbon nuclei. In coincidence with the 15 MeV gamma, we see a number of multiplicity two events in the Lampshade, in opposite sectors; as

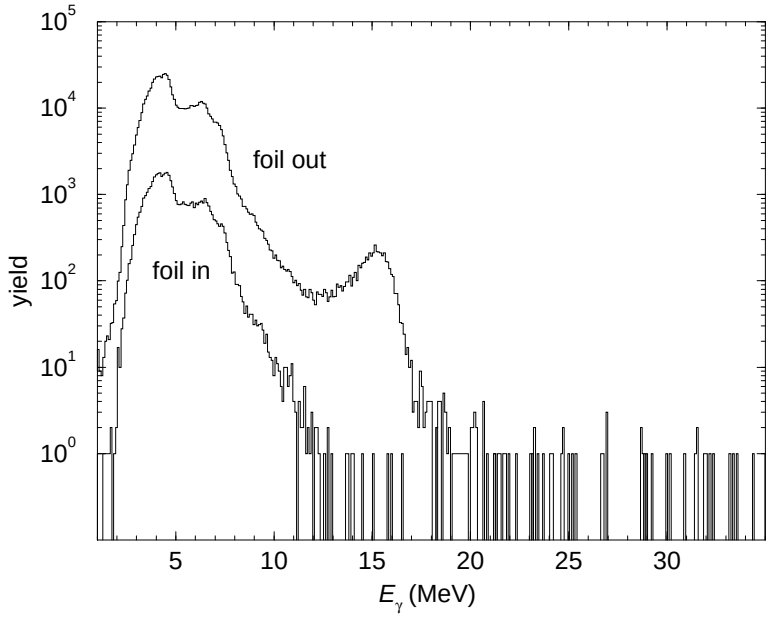

Figure 3.14: *Gamma-particle coincidence spectra with and without stopper foil*

we would expect, the two carbons are in-plane with the beam axis. In fig. 3.19 the numbering of the Lampshade sectors is shown; a pair of opposite sectors with numbers n_1 and n_2 is characterised by $|n_1 - n_2| = 3$—a peak is seen here in the spectrum of $|n_1 - n_2|$. Two peaks are seen in the spectrum of opening angles for lamp-lamp-γ_{15} events, corresponding to the two transitions. The summed energy spectrum shows a broad peak with a low energy tail—or two unresolved peaks corresponding to the Q-values of the two transitions. The poor resolution in this spectrum can be attributed to the energy loss in the target.

Not all the events in coincidence with the 15 MeV gamma contain both carbons however—the detector geometry and kinematics mean that LEDA-LEDA or LEDA-Lampshade coincidences are not possible for this reaction. Furthermore, about half of the Lampshade-γ_{15} coincidence events contain only one particle, because the second carbon is sometimes stopped either in the target or the detector's dead layer, or suffers energy loss such that it is below threshold in the detectors.

It is therefore also necessary to include events with one particle in the Lampshade array. Figure 3.18 illustrates events that appear in LEDA, contrasted with those that are observed as Lampshade-Lampshade coincidences.

The measured cross-sections from the first run are shown in figure 3.17. The LEDA-Lampshade measurements at 45 MeV can be seen in figure 3.20. The measurements from the third run, using the LEDA-Lampshade configuration at 29.5 MeV, agree very well with those from the first experiment, giving a data set for this energy running from 6° to 32°. Figure 3.21 shows this combined data set.

In the next chapter the use of the simulation code `fresco` will be described and its output compared to the experimental data shown above.

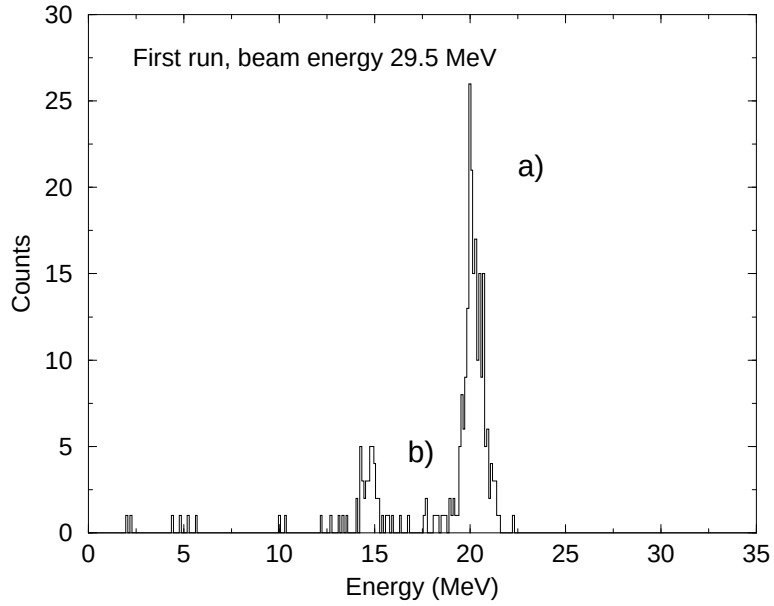

Figure 3.15: *LEDA spectrum at $\theta_{lab} = 21^o$, gated on 15 MeV gamma peak*

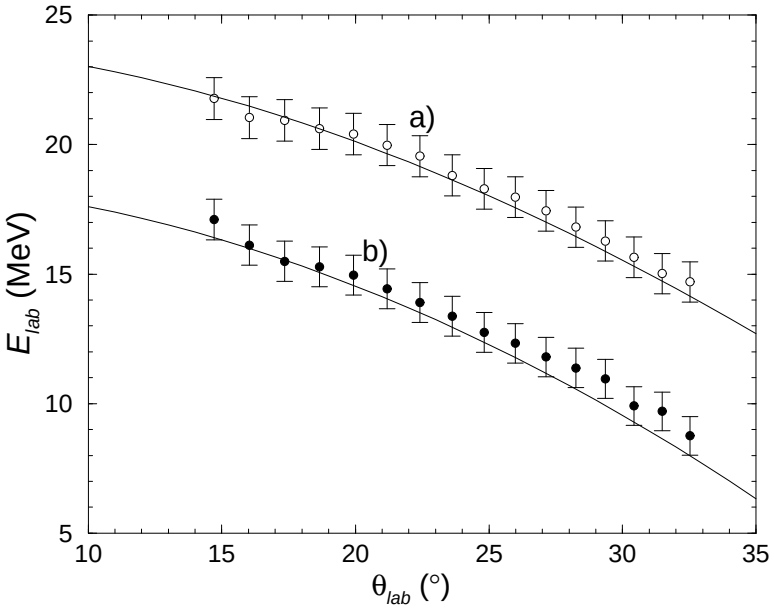

Figure 3.16: *Angular dependence of the energy of the peaks in fig. 3.15, and the kinematics calculation of Appendix A*

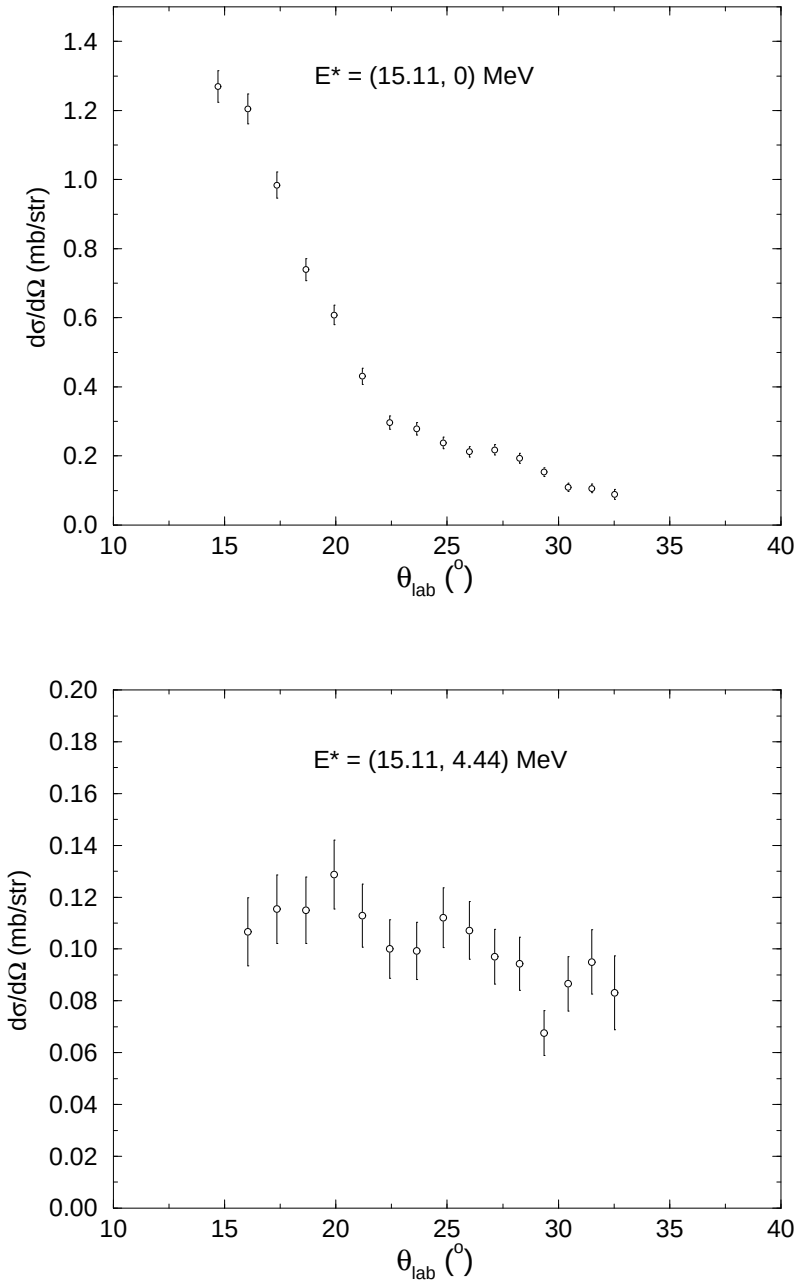

Figure 3.17: *Angular distribution of peaks a) and b) in fig. 3.15*

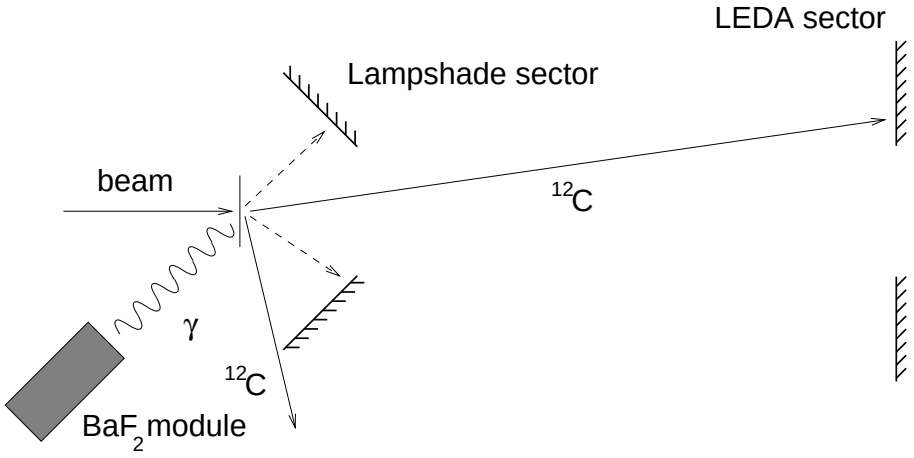

Figure 3.18: *Illustration of detection of* $^{12}C - ^{12}C - \gamma$ *events*

Solid lines: LEDA event; Dashed lines: Lampshade-Lampshade coincidence

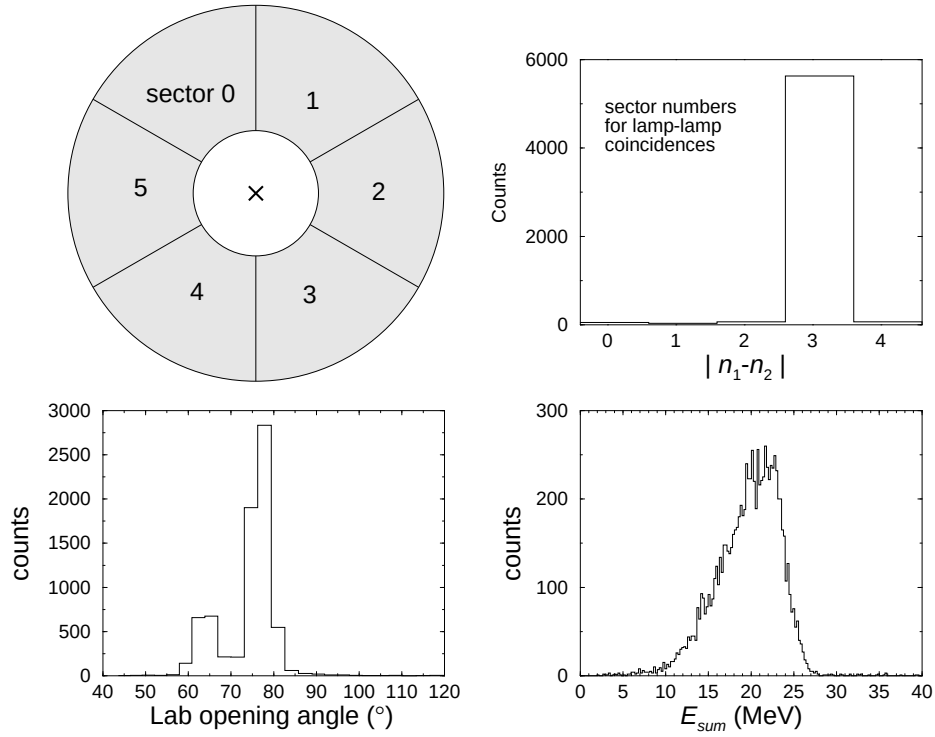

Figure 3.19: *Energy and distribution of lamp–lamp–*γ_{15} *coincidences*

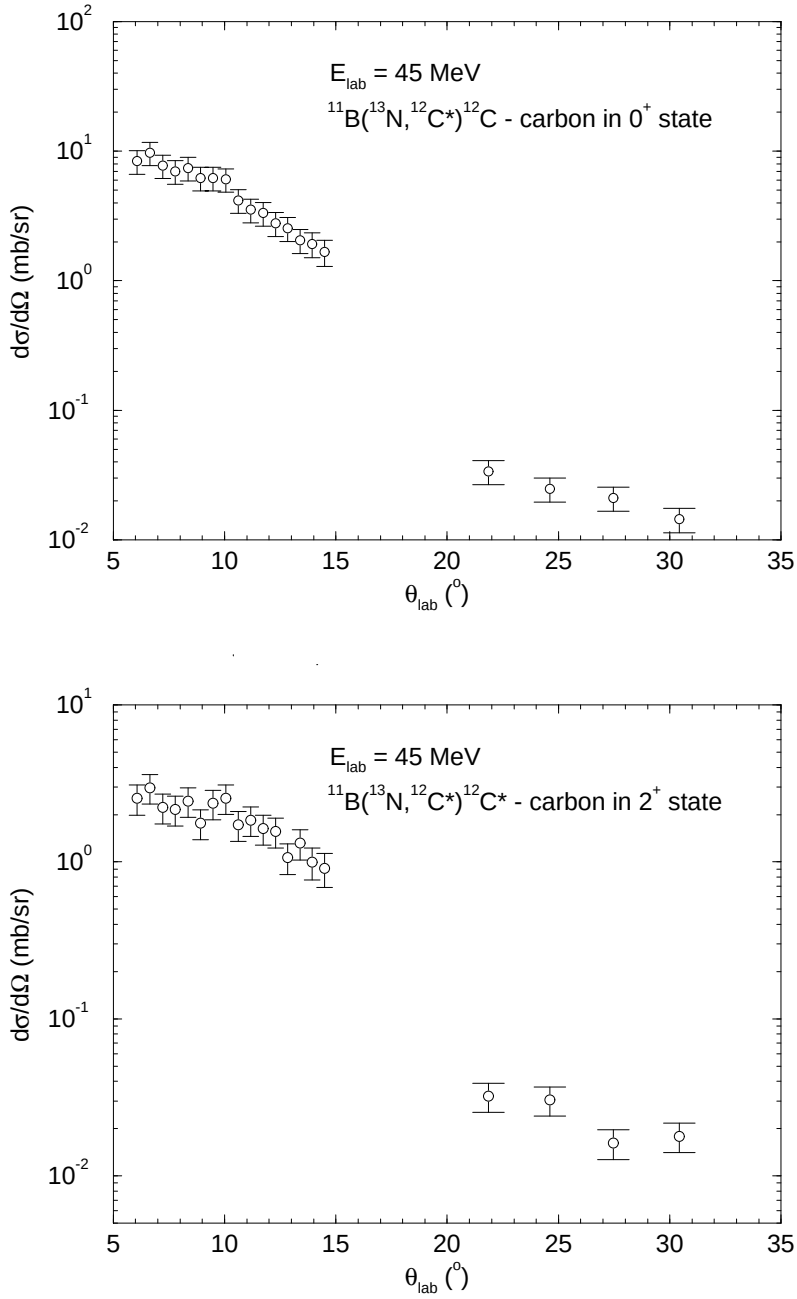

Figure 3.20: *Differential cross section of transfer reaction, 45 MeV*

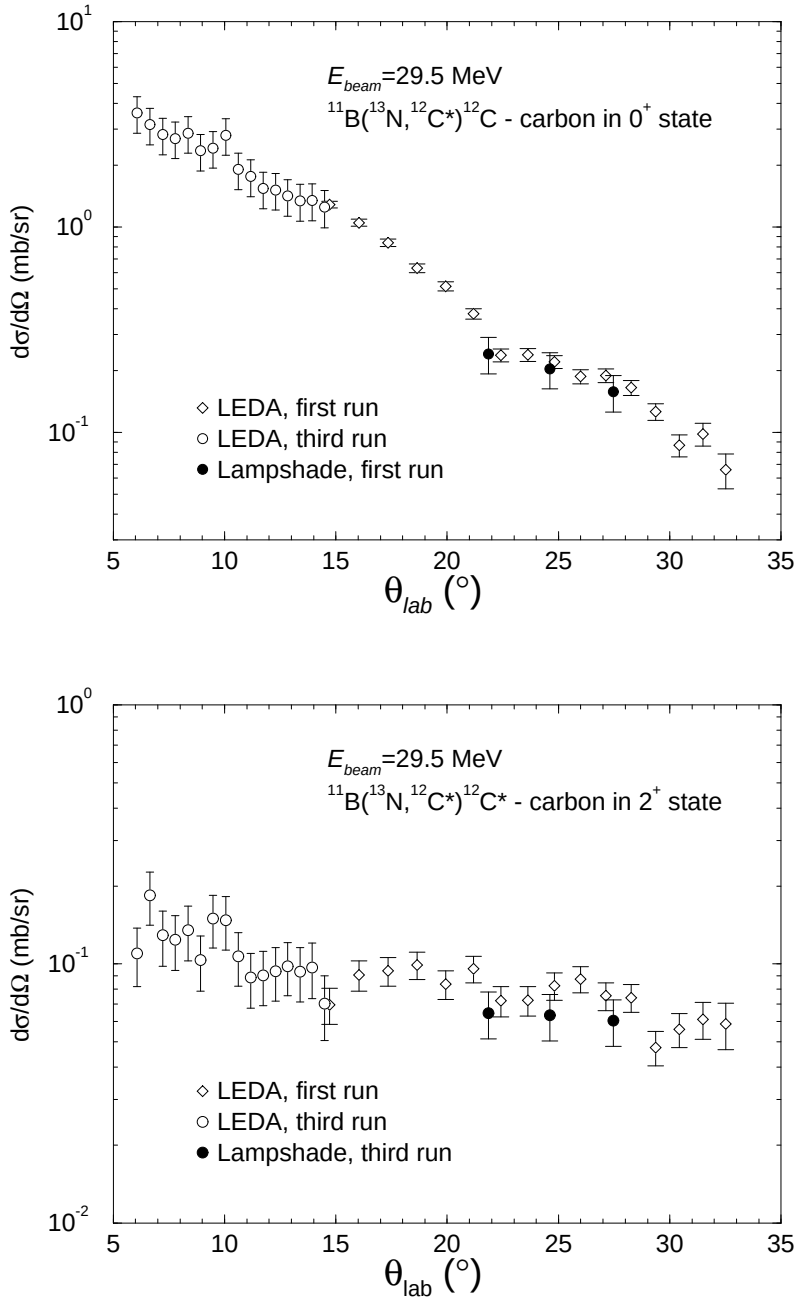

Figure 3.21: *Differential cross section of transfer reaction, 29.5 MeV*

Chapter 4

Theoretical Interpretation

4.1 Introduction

The measured cross sections for the heavy ion plus gamma coincident events are characteristic of transfer reactions above the Coulomb barrier, although the arrangement of the detectors was such that the peak at very forward angles was not seen, and the "diffraction" pattern of structure that is often seen in the angular distributions of transfer reactions appeared to be absent.

In order to attempt to interpret the experimental results in terms of an existing theory of nuclear reactions, the code `fresco`, written by Thompson [57, 58] has been applied to the reaction examined in these experiments. This chapter will describe these calculations and their results, and discuss the success with which they reproduce the data.

`fresco` is a general case Coupled Reaction Channels (CRC) code in the framework of Direct Reaction theory. The program can solve for exact finite range transfers (EFR) in one or two-step Distorted Wave Born Approximations (DWBA), or by iteration for multistep processes. It supercedes many earlier codes which dealt with one or two-step DWBA, or with zero-range transfers, or for a limited range

of entrance channels, and provides a more general solution for CRC calculations. For an example of a previous successful comparison between experimental data and predictions made by `fresco`, see the work of Kerr *et al* [59], which also makes a favourable comparison with the cross sections generated by the earlier code `chuck3` [60].

4.1.1 Optical Model Fits

The fitting of elastic and inelastic scattering or transfer data with DWBA codes using complex optical model potentials is a standard tool in heavy ion reaction physics. A complex central potential is used to represent the nuclear interaction:

$$U(r) = V(r) + i\,W(r) \tag{4.1}$$

The Woods-Saxon (W-S) form is commonly used to parametrise the complex potential:

$$\begin{aligned} V(r) = &\quad -V_0\, f_r(r) \\ W(r) = &\quad -W_0\, f_i(r) \end{aligned} \tag{4.2}$$

$$f_x(r) = \left[1 + \exp\left(\frac{r - R_x}{a_x}\right)\right]^{-1} \tag{4.3}$$

$$R_x = r_{0x}(A_1^{1/3} + A_2^{1/3})$$

where the subscripts r and i denote real or imaginary. The real potential is the nuclear interaction, and the imaginary part is included to represent absorption, *ie* the loss of flux from the elastic channel.

The Coulomb interaction is taken to be that for a uniformly charged sphere of radius R_C:

$$V_C(r) = \begin{cases} \dfrac{Z_1 Z_2 e^2}{r} & \text{for } r > R_C \\ \dfrac{Z_1 Z_2 e^2}{R_C}\left(\dfrac{3}{2} - \dfrac{1}{2}\dfrac{r^2}{R_C^2}\right) & \text{for } r < R_C \end{cases} \tag{4.4}$$

$$R_C = r_{0C}(A_1^{1/3} + A_2^{1/3})$$

The quality of the fit is usually determined by calculating χ^2 or a similar quantity for the N data points:

$$\chi^2 = \sum^{N} \left(\frac{\sigma_{\rm ex} - \sigma_{\rm th}}{\delta\sigma_{\rm ex}} \right)^2 \tag{4.5}$$

where $\sigma_{\rm ex}$ and $\sigma_{\rm th}$ are the measured and theoretical values of the cross section and $\delta\sigma_{\rm ex}$ is the uncertainty in $\sigma_{\rm ex}$. The value of chi-squared per degree of freedom can also be defined, as χ^2/N_F, where N_F is the number of data points minus the number of free parameters in the fit. A judgement by eye of the quality of fit can often be more reliable than comparing values of χ^2, though, particularly if they are large.

However, finding the best fit is not always as simple as finding a minimum in χ^2; there are often ambiguities to be found in these fits, in the physical interpretation of the parameters used, and also because a family of potentials with different parameters can often be found which have equal success at reproducing the experimental data. With potentials of this type there is the well known VR^n ambiguity (different parameter sets can give equally good fits if there are small variations in V_0 and r_{0r} such that $V_0 r_{0r}^n$ is constant, where $n \approx 2$ [61, page 500]). A similar ambiguity exists for $W_0 r_{0i}^n$, and for other combinations of the parameters, so that in parameter space there are many local minima in the value of χ^2 for the fit. Direct one-step reactions such as the one-proton transfer studied here are usually most sensitive to the tail of the potential, which in turn is likely to be insensitive to small variations in the parameters. Fitted potentials can also show discrete ambiguities, with real parts whose depth is a roughly integer multiple of some minimum. It has been suggested that under certain circumstances the ratio of the real and imaginary parts of the complex potential, $V(r)$ and $W(r)$, is the significant quantity [62], which implies another kind of ambiguity. Ambiguities in optical potential fits are discussed in detail in ref. 63, page 153.

4.2 Surrey Calculations

Subsequent to the experimental data being obtained, preliminary calculations on the (^{13}N,^{12}C*) reaction were carried out by J.A. Christley at the Surrey nuclear physics group [24]. A Woods-Saxon form was used for the distorting potential, and the parameters used (set #1 in table 4.1) were those fitted by Voos *et al* [64] to elastic scattering data of ^{11}B+^{12}C at 28 MeV. The same geometry of distorting potential (except with a core mass of 11) is used for the exit channel, where the $^{12}C^*_{15.11}$ state is constructed as $|^{11}\mathrm{B} \otimes 1\mathrm{p}_{\frac{1}{2}}\rangle$. This state has S_p=0.82 MeV and the calculated mean proton-core separation is 3.48 fm.

Core-proton states $|^{12}\mathrm{C}(0^+) \otimes 1\mathrm{p}_{\frac{1}{2}}\rangle$ and $|^{12}\mathrm{C}(2^+) \otimes 1\mathrm{p}_{\frac{3}{2}}\rangle$ are specified, and the code generates proton wave functions, scaling them to reproduce the empirical proton binding energies (1.956 MeV and 1.956+4.44=6.396 MeV) for each of the two core states. The radial proton wave functions are shown in fig. 4.1, as well as that for the valence proton in ^{12}C*; note that the spectroscopic factors are not included here—the wave functions are normalised so that $\int u^2\, dr = 1$. The RMS radius of the proton distribution, for the $\mathrm{p}_{1/2}$ state in particular, is significantly larger than the interaction radius of ^{12}C, 2.61 fm [65]. The tail of the proton distribution is clearly more pronounced in the $\mathrm{p}_{\frac{1}{2}}$ state than in the more tightly-bound $\mathrm{p}_{\frac{3}{2}}$ state—which might lead us to suppose that, other factors being equal, at more forward angles the transition to $^{12}\mathrm{C}_{0^+}$ would be favoured over that to the first excited state. Spectroscopic factors also need to be considered, however; the relative cross sections will depend on how the different proton-core states mix in the ^{13}N ground state. The results of the Surrey calculations of the differential cross sections for each energy and each of the final states in ^{12}C, can be seen in fig. 4.2. The cross sections of the 2^+ transition clearly show the beam energy dependence—the Q-matching is better at the higher energy for this transition.

The initial work done at Surrey on this reaction also included a consideration of coupled channel effects between the 0^+ and 2^+ states in ^{12}C, to account for the

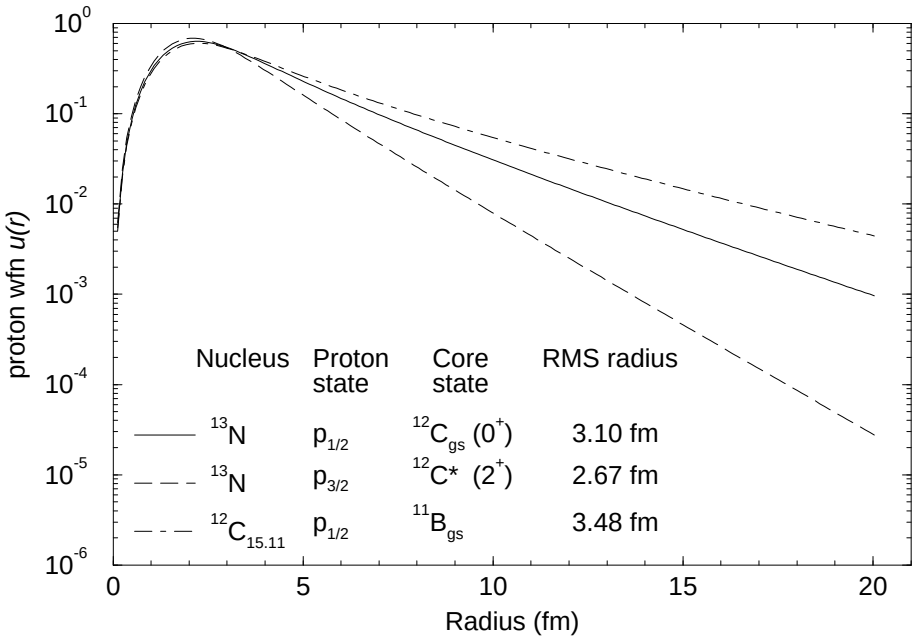

Figure 4.1: *Valence proton wave functions in ^{13}N and ^{12}C*

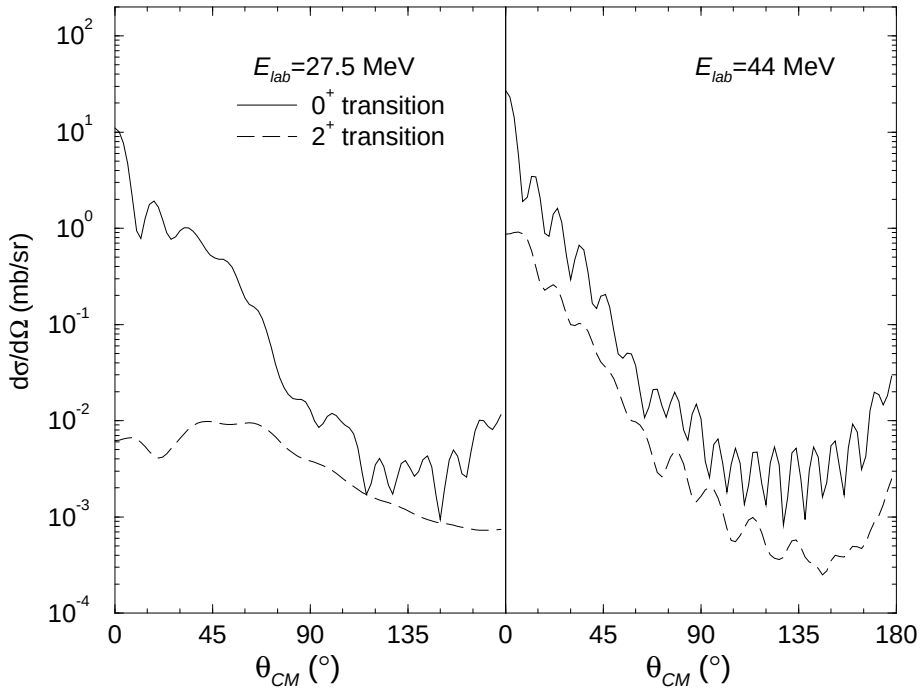

Figure 4.2: `fresco` *calculations from Surrey*

NB spectroscopic factors not included.

possibility of excitation and de-excitation of the ^{12}C in the final state. However the report of ref. [24] concludes that these effects would be small and had little impact on the calculated angular distributions.

Alternative Sets of Potentials

The literature gives several sets of fitted potentials for ^{12}C+^{11}B (see table 4.1). Note that the authors all report that the fits are insensitive to r_{0C}; commonly used values are 1.25 fm to about 1.4 fm. The real and imaginary parts of the complex potential are shown in figure 4.3; it can be seen that the tails of the potentials are very similar for each set.

A comparison of `fresco` output using these sets of parameters is shown in fig. 4.4. The magnitude and gross behaviour of the transfer differential cross sections appear to be the same for each of the sets of potentials, although the position and strength of the oscillations changes somewhat.

#	V_0	r_{0r}	a_r	W_0	r_{0i}	a_i	System		Ref.
	(MeV)	(fm)		(MeV)	(fm)			E_{lab}	
1	50	1.29	0.48	15	1.18	0.30	^{11}B+^{12}C	28 MeV	64
2	100	1.19	0.48	27	1.26	0.26	^{11}B+^{12}C	28 MeV	64
3	100	1.19	0.47	27	1.29	0.30	^{12}C+^{11}B	24 MeV	66
4	100	1.23	0.43	29.5	1.19	0.20	^{11}B+^{12}C	28 MeV	67

Table 4.1: *^{12}C +^{11}B Woods-Saxon potentials from the literature*

4.3 Comparison With Experimental Data

In comparing the `fresco`-generated cross sections with the experimental data, the sensitivity of the experimental method must be considered. The angular resolution

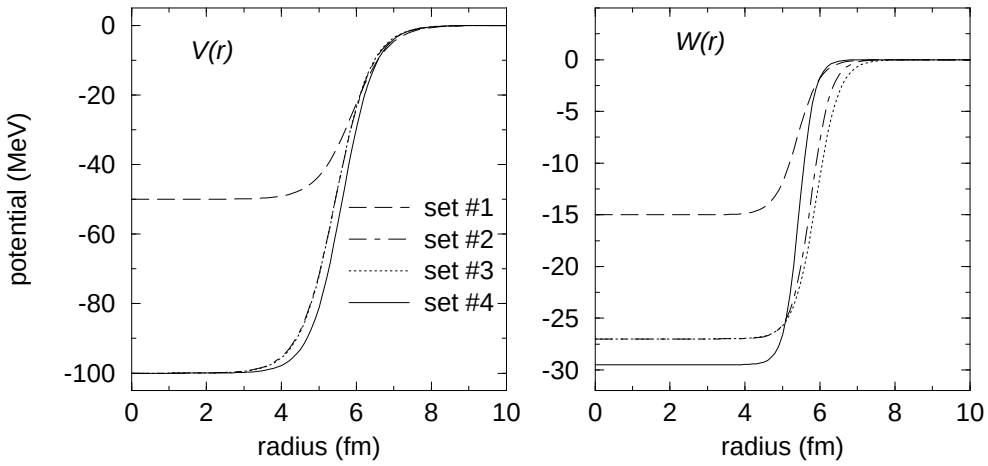

Figure 4.3: *Potential forms with parameter sets from table 4.1.*

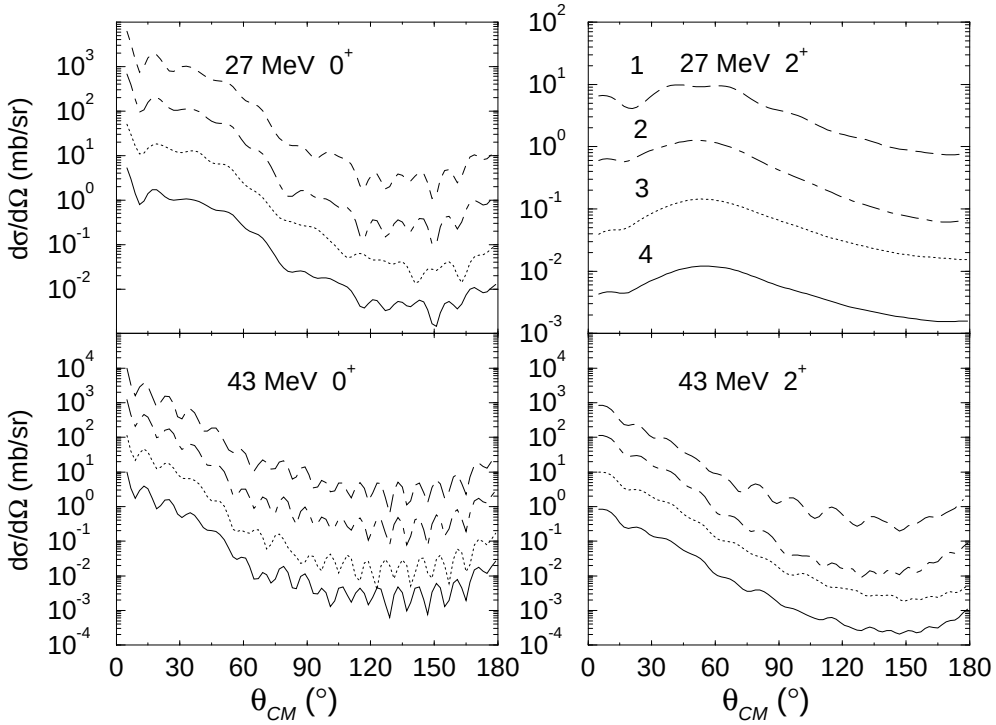

Figure 4.4: `fresco` *output using potential sets #1–4 in table 4.1. For clarity, the curves for sets 1–3 have been multiplied by factors* 10^3, 10^2 *and 10 respectively. Legend is as figure 4.3.*

of the detectors must be taken into account before details such as the distributions' oscillatory nature can be examined, and also the energy dependence, since the thickness of the target introduces a certain energy width. These two effects, finite θ resolution and target thickness, will tend to smear out the distributions in the experimental data.

The energy loss experienced by ^{13}N in the target is expected to be about 4 MeV; figure 4.5 shows the results of a number of `fresco` runs, using the original Surrey parameters, for different lab energies, ranging from 29.5 MeV down to $29.5 - 4 = 25.5$ MeV. The dashed line is the average of runs at 25.5, 26.5, 27.5, 28.5 and 29.5 MeV; for the sake of clarity only the distributions for the two extreme cases, 25.5 and 29.5 MeV, are shown (continuous curves).

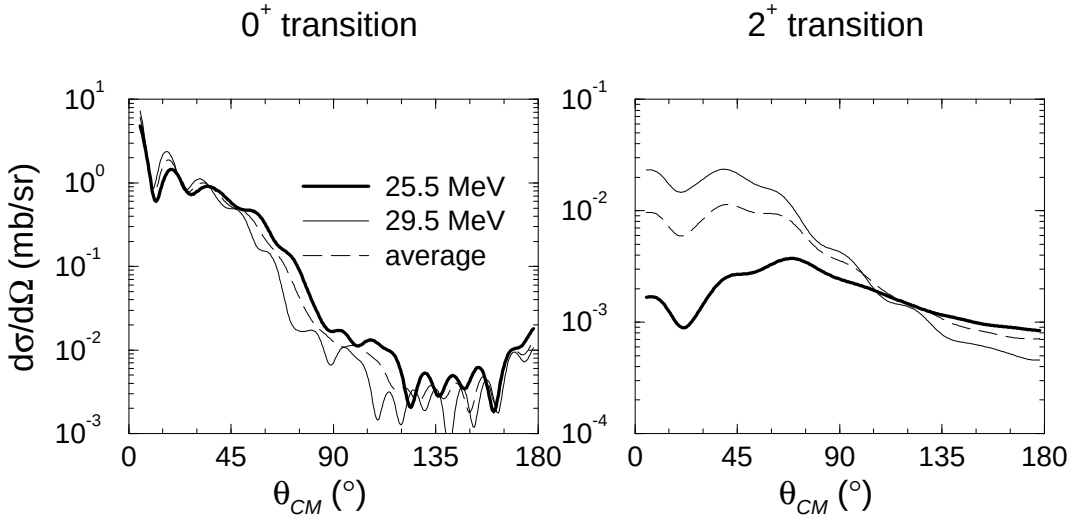

Figure 4.5: `fresco` *output for various beam energies, showing the effect of finite target thickness on the cross sections.*

The strength of the transition to the 2^+ state in ^{12}C, in particular, is very energy-dependent, reflecting the effect of Q-matching. The smearing effect of the thickness of the target is smaller at the higher energy, 45 MeV, because the cross sections are less energy-dependent in this region. In addition, the energy thickness of the target is smaller, because the faster beam particles experience less energy loss.

Once the cross sections have been averaged over energy, they are integrated over the geometry of the detector elements. Figure 4.6 shows the effect of this; the points are the average values for each strip in LEDA and the Lampshade, the solid line is the actual distribution.

As mentioned in Chapter 3, the unusual geometry of the Lampshade makes it necessary to consider carefully the question of where the 'centre' of a particular strip is taken to be; the form of the distribution being measured, and the shape of the detector element have to be taken into account. The `fresco` predictions, and the measured cross sections were observed to fall off roughly exponentially with θ (with the exception of the 2^+ data at 29.5 MeV, which was more or less constant). An exponential fall off was therefore used in a procedure similar to that employed to calculate the Lampshade solid angle, as described in Chapter 3; the exponential distribution was imposed on the previously isotropic hypothetical particles that were tracked to the detector. The mean value of θ of all the particles incident of each strip was taken to be the mean angle for that strip, and the value at which the data should be plotted. This value turned out to differ from the central value of θ by no more than 0.5^o in the Lampshade; in LEDA the effect was negligible.

It is clear, that, for the arrays at more forward lab angles, the detector geometry and energy width do not appreciably affect the experimental sensitivity to features in the distributions, or at least those in the calculated cross sections. The Lampshade array is a little coarser in θ_{lab}—but at the more backward angles that it covers the predicted distributions are less oscillatory anyway.

The distributions can now be directly compared with the experimental results (fig. 4.7). These plots include the proposed spectroscopic factors $|\alpha|^2 = 0.3195$ and $|\beta|^2 = 0.6704$ (see Chapter 1), which have been applied to the calculated cross sections.

The oscillatory behaviour in the calculated cross sections is notably absent from all the measured cross sections. For the 0^+ transition at the lower beam energy,

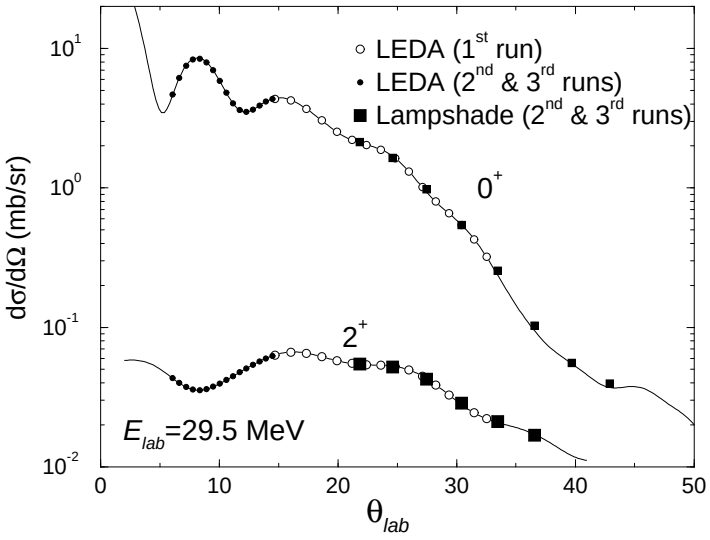

Figure 4.6: `fresco` *transfer reaction cross sections folded with detector resolution. The continuous line is the actual predicted cross section, the points are the apparent cross sections that would be measured by the detector elements in the LEDA and Lampshade arrays.*

the magnitude and gross trend in the angular distribution is reproduced quite well, but the calculation badly under-estimates the strength of the 2^+ transition; again, however, the general trend is correct—the cross section is more or less constant over the angles for which measurements were taken.

At the higher beam energy, 45 MeV, the code predicts stronger oscillations, which again are absent, and this time the trend above $\theta_{CM} > 40^o$ is less well predicted; there is a sharp fall in cross section which is not seen in the theoretical curves.

4.4 Obtaining a More Successful Fit to the Data

The calculations described above were made using the potentials used to fit ^{11}B+^{12}C elastic scattering at 28 MeV, a reasonable starting point for the in-

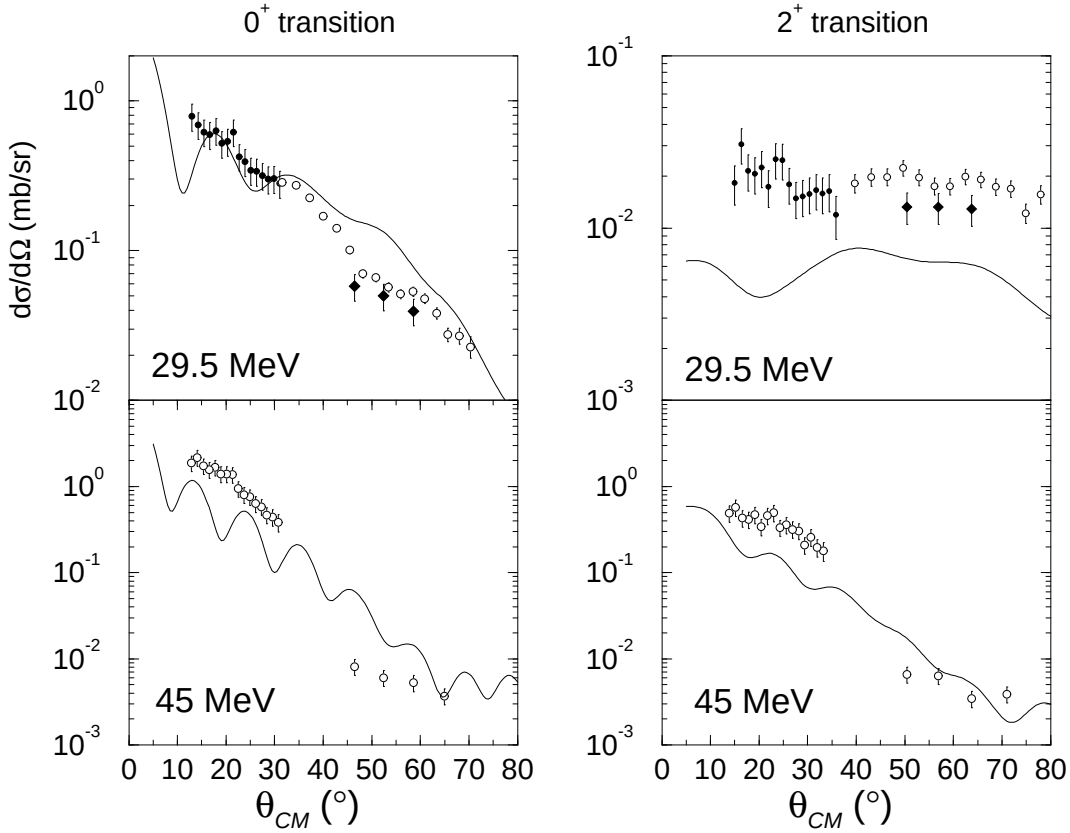

Figure 4.7: *Measured and predicted transfer reaction differential cross sections. The calculated angular distributions use the Voos potentials, set #1 in table 4.1.*

terpretation of the present data. However, we should not be surprised if there are differences between a set of data and calculations using parameters that are an empirical fit to reproduce experimental data from a slightly different reaction. In view of this, these potentials can be considered to have been rather successful in predicting the magnitude and gross behaviour of the angular distributions. However, it would be desirable to obtain a closer agreement between theory and experiment, or at least to be able to explain the observed differences.

As part of the present work, therefore, and following on from the Surrey calculations, some of the code's input parameters have been varied, in order to obtain a set of predicted differential cross sections that are in better agreement with the experimental data.

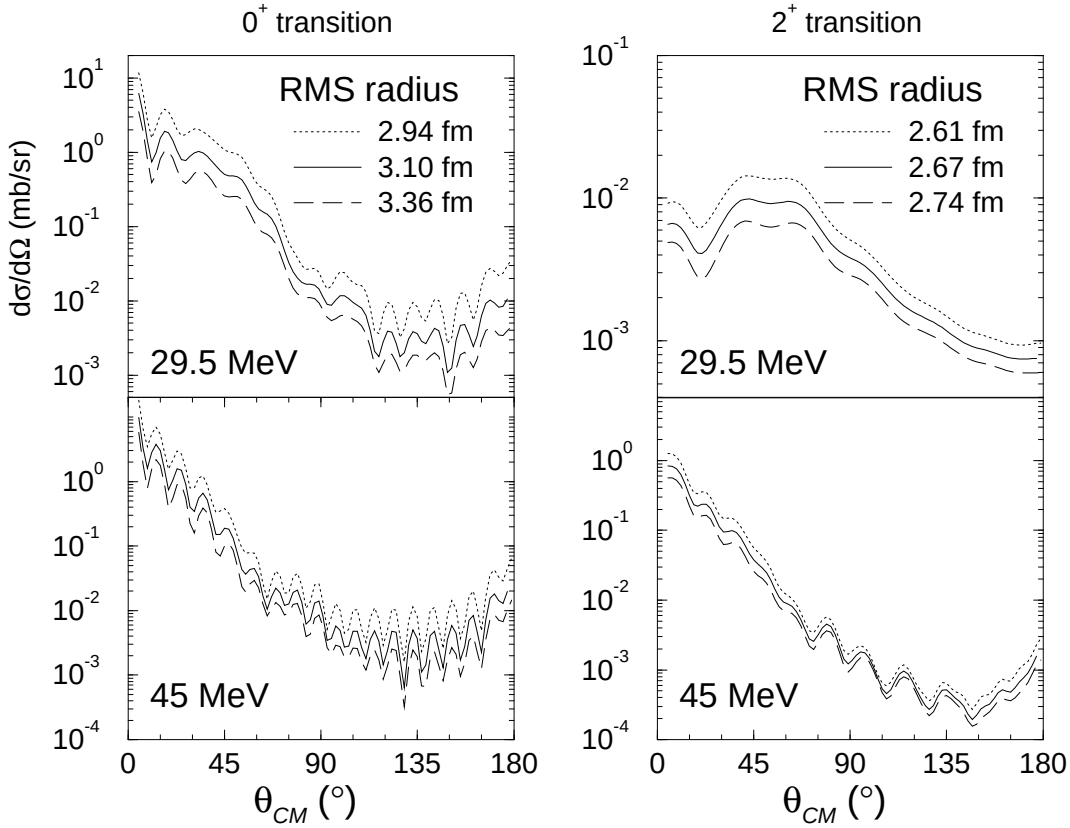

Figure 4.8: *The effect of more and less extended proton wave functions on* `fresco` *calculations. Top: Calculations for beam energy 29.5 MeV. Bottom: 45 MeV. The optical potentials used are those of Voos.*

4.4.1 Sensitivity to the Proton Wave Function

One possible reason for the discrepancy between measurements and predictions is the expected sensitivity of the transfer cross sections to the extended wave function of the least bound proton. It is possible to explore this sensitivity by introducing alternative wave functions, which differ in the value of $\langle r^2 \rangle^{\frac{1}{2}}$, into the calculations. Figure 4.8 shows the results of calculations made using the new wave functions, which have RMS radii of of 2.94 fm and 3.36 fm for the $p_{\frac{1}{2}}$ state (compared to 3.10 fm originally), and in the $p_{\frac{3}{2}}$ state, 2.61 fm and 2.74 fm (compared to 2.67 fm).

It appears that the strength of the transition is strongly affected by the RMS radius of the proton wave function—a slightly more extended distribution such as used here gives a much higher (by a factor of 2) cross section, and *vice versa*—but the shape of the angular distribution is largely unaffected. The cross sections shown above are for calculations where the RMS proton-core separation for the the least bound proton in $^{12}C^{*}_{15.11}$ (or $^{11}B \otimes p_{\frac{1}{2}}$) is left at the original value of 3.48 fm, but changing this value, in combination with that of the ^{13}N valence proton, or by itself, does not appreciably affect the behaviour of the transfer cross sections.

4.4.2 $^{13}N+^{12}C$ Elastic Scattering

In trying to model a reaction of ^{13}N, it is appropriate to consider the clues provided by previous successful fits to some of its other reactions. An interesting comparison can be made here between the data from Liénard *et al* and `fresco` calculations on $^{13}N+^{12}C$. The optical model parameters suggested in ref. 25 for $^{13}N+^{12}C$ and $^{13}C+^{12}C$ elastic scattering are shown in table 4.2. Two sets are given, differing mainly in depth. These sets of parameters both contain slightly higher values of real diffuseness than the fits to $^{12}C(^{11}B,^{11}B)$ data, and the imaginary diffuseness is significantly higher; this is a possible reflection of the spatial extent of the valence nucleon in ^{13}C and ^{13}N. Figure 4.9 shows the $^{13}N+^{12}C$ elastic scattering data of Liénard *et al* and `fresco` calculations using their optical model parameters. We see that the agreement with the data is excellent for the shallow set, at forward angles (the angles for which the transfer reaction on ^{11}B has been measured, $\theta_{CM} < 75^{o}$). At backward angles the agreement breaks down, although the treatment by Liénard *et al* (which gives a good fit in this region) includes a parity term $(-)^{l}V_{p}$ [68,69], the sign of which depends on whether a particular partial wave is odd or even, and it appears that this becomes significant above 90^{o}, where elastic transfer starts to make a significant contribution to the cross section. In any

case there is no available data for ^{11}B(^{13}N,^{12}C)^{12}C* above 75°, and elastic transfer does not concern us here. The success of the shallow potential for ^{13}N+^{12}C lends support to the idea of fitting a shallow potential to ^{13}N+^{11}B, despite the ^{12}C+^{11}B parameters taken from the literature being rather deeper. Applying a similar, reduced imaginary potential to optical fits to ^{13}C+^{11}B might have been a useful approach to modelling the transfer reaction on ^{13}N+^{11}B, but unfortunately no such fits have been published.

The difference in the imaginary potentials for the ^{13}N case compared with ^{13}C has also been discussed by Imanishi *et al* [70].

4.4.3 Shallow Potentials

The question of the absence of the usual diffraction type patterns in the measured cross sections can be approached in several directions. We have already seen that the tail of the valence proton wave function does not appear to be significant in this regard. The obvious possibility to consider is that the optical potential being used is inappropriate, bearing in mind their origin.

For the reasons explained in Chapter 3, elastic scattering data was difficult to extract, and so it was not possible to obtain a systematic fit to such data using the optical model fitting codes that are available. The six parameters of the optical potential were therefore varied independently and the transfer reaction cross sections produced by using each set of parameters in the `fresco` code were compared with the experimental data. The criterion for quality of fit that was used was χ^2, as defined in (4.5), applied to the 0^+ data at the lower beam energy. In view of time constraints on the computationally intensive calculations being made it is possible that the sets of potentials that were obtained are not unique in their quality of fit, *ie* that there are other combinations of parameters that would also produce local minima in χ^2.

#	V_0	r_{0r}	a_r	W_0	r_{0i}	a_i	System	
	(MeV)	(fm)		(MeV)	(fm)			E_{lab}
5	115.8	1.09	0.50	22.1	1.09	0.51	^{13}C+^{12}C	29.5 MeV
6	115.8	1.09	0.50	8.6	1.09	0.51	^{13}N+^{12}C	
7	16.6	1.28	0.56	17.3	1.26	0.44	^{13}C+^{12}C	
8	16.6	1.28	0.56	3.0	1.26	0.44	^{13}N+^{12}C	

Table 4.2: *^{13}N,^{13}C +^{12}C deep and shallow optical potentials of Liénard* et al

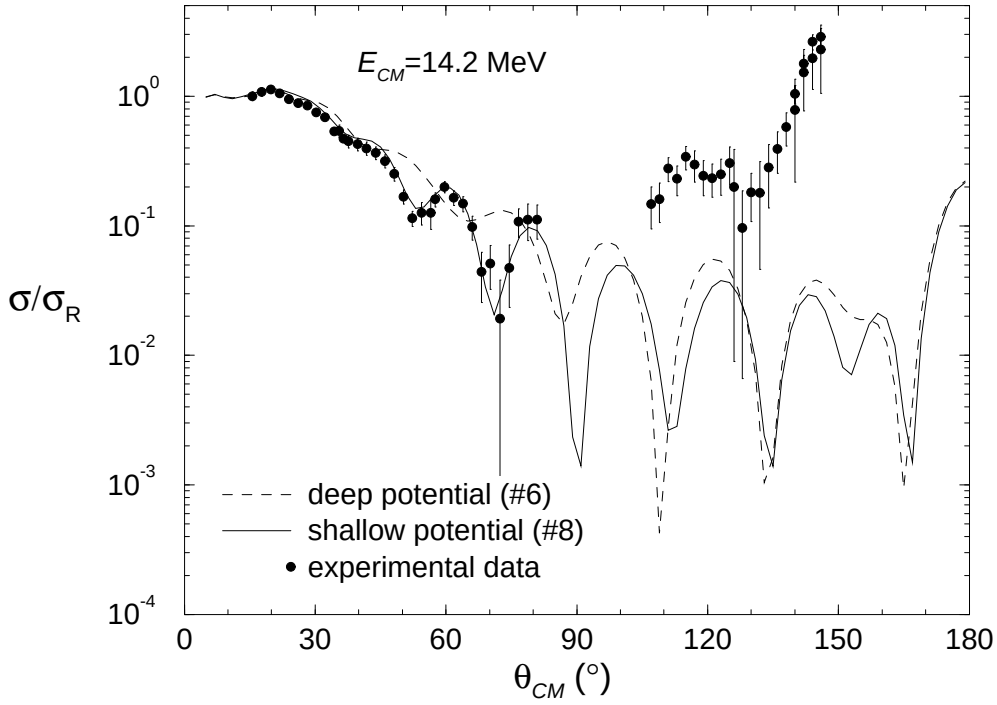

Figure 4.9: *Rutherford ratio of ^{13}N +^{12}C elastic scattering: Experimental data and* `fresco` *calculations, using the potentials of table 4.2.*

It was found that using a drastically more shallow potential than the ones previously considered gave somewhat better agreement to parts of the measured data, going some way to eliminating the strong oscillations seen in the cross sections produced by the initial calculations. The curve shown in fig. 4.10 gives a value of χ^2/N_F of 4.9 for the 0^+ transition at $E_{lab} = 29.5$ MeV, compared to 61 for the Voos potentials. The agreement for the 2^+ transition with this set of potentials is worse, however; the magnitude and shape of the angular distribution are incorrectly predicted.

Having found a better agreement with a shallow potential for the lower beam energy, the value of V_0 was fixed and the other parameters were varied in order to obtain a shallow potential fit to the 0^+ at 45 MeV data. It was found that the quality of the fit was insensitive to adjustments in the real and imaginary diffusenesses of up to 20%, but it was necessary to change the imaginary depth and the real and imaginary radius parameters. Figure 4.11 illustrates the results of this procedure; both the 0^+ and the 2^+ cross sections agree with the code's prediction quite well. It is noted that the agreement of fit is clearly energy-dependent; each of the two sets of parameters, as shown in figures. 4.10 and 4.11 only gives reasonable agreement for data at one of the beam energies for which data was taken.

The greater strength of the imaginary potential at the higher beam energy is not unexpected; when more energy is available, more states, at higher excitations, become accessible, and so the absorption is greater.

4.5 Resonances in ^{12}C+^{12}C

One aspect of the reaction mechanism that might alter the cross sections from what would be expected from a straightforward, one step direct transfer, is the possibility of some kind of resonance. There are several well known resonances

Beam energy	V_0	r_{0r}	a_r	W_0	r_{0i}	a_i
29.5 MeV	5.0	1.50	0.53	4.3	1.50	0.67

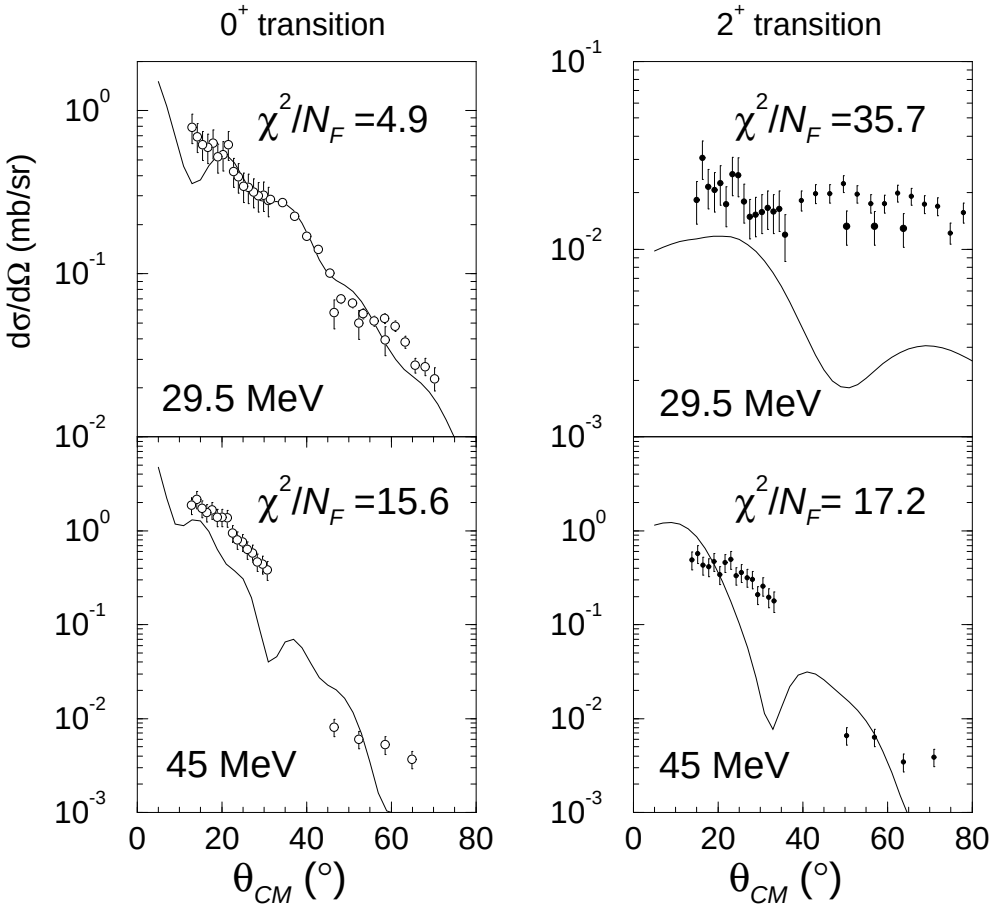

Figure 4.10: *Transfer cross sections for the* 0^+ *(left) and* 2^+ *(right) transitions using the above shallow optical potentials, for beam energy 29.5 MeV (top), compared with experimental measurements. Also shown are the cross sections at 45 MeV calculated using these potentials.*

Beam energy	V_0	r_{0r}	a_r	W_0	r_{0i}	a_i
45 MeV	5.0	1.40	0.53	10	1.20	0.67

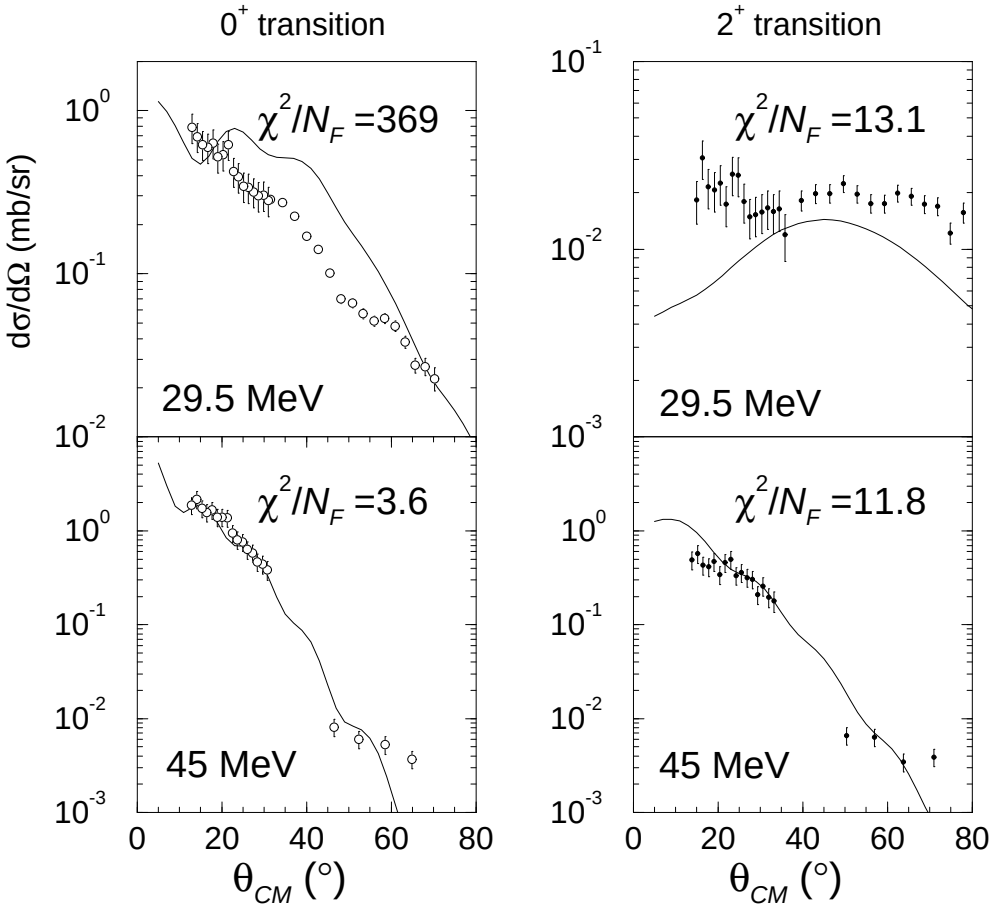

Figure 4.11: *Transfer cross sections for the 0^+ (left) and 2^+ (right) transitions using the above shallow optical potentials, for beam energy 45 MeV (bottom), compared with experimental measurements. Also shown are the cross sections at 29.5 MeV calculated using these potentials.*

in $^{12}C_{gs}+^{12}C_{gs}$ near the Coulomb barrier (*ie* around 6.5 MeV), the first of which were observed in the early days of heavy ion physics by Bromley *et al* [71, 72]. These resonances are characterised by their narrow width ($\Gamma \approx 100$ keV) and have values of $J^{\pi} = 2^+, 4^+, 6^+$, *etc.* This energy region corresponds to around 20 MeV of excitation in the compound nucleus ^{24}Mg, where there is a near continuum of states. The level density is hundreds per MeV, whereas the resonances are isolated (10 or so per MeV) and sharp. In addition, the partial widths Γ_C for $^{12}C+^{12}C$ in the exit channel are an order of magnitude higher than what we would expect for heavy evaporation residues from a highly excited compound nucleus, with Γ_C/Γ typically around 10 % [73, page 211]. Clearly, therefore, these resonances have a kind of structure quite different to that of the ordinary states around 20 MeV in $^{24}Mg^*$.

A similar phenomenon involving $^{12}C_{2^+}+^{12}C_{1^+}$ could perhaps provide a modification to the transition probability. It is plausible to suppose that such a state could be reached in the present data; in the present work the center of mass energy of $^{12}C_{2^+}+^{12}C_{1^+}$ in the exit channel is scanned through values between about 6 and 8 MeV (because of the finite thickness of the target). Several resonances have been observed at similar $^{12}C+^{12}C$ centre of mass energies. Of particular interest in this context is the work of Cormier and Fulton [74], which examines the structure to be seen in the excitation functions of the transfer reactions $^{12}C(^{12}C,^{10}B)^{14}N$ and $^{12}C(^{12}C,^{11}B)^{13}N$. Several resonant structures are seen, in the $^{10}B+^{14}N$ channel in particular, which correspond to previously observed resonances which are interpreted as molecular states of $^{12}C_{2^+}+^{12}C_{0^+}$ and $^{12}C_{2^+}+^{12}C_{2^+}$. The presence of such structure in the excitation function when the final state is $^{11}B+^{13}N$ state is less obvious in the data of ref. 74, however.

In a similar vein, the reaction at the higher beam energy, 45 MeV, also happens to access an energy region (supposedly) occupied by an unusual phenomena associated with $^{12}C+^{12}C$. At this energy the excitation in the compound nucleus, ^{24}Mg, is around 48 MeV, almost exactly the energy at which the 6α chain state

has been searched for [75]. Preliminary analysis by Di Pietro of the multiplicity six events in this data shows a measurable yield of 6α events [76], but whether or not they originate in a chain state is thus far unresolved. It might have been thought possible that in the $^{13}N+^{11}B$ reaction at this energy the proton transfer could act as a door-way into the chain state, reducing the final yield of $^{12}C+^{12}C$; however, given the success of the DWBA calculations at this energy, there is no evidence of this in the present work. If there is any yield of the 6α chain state in this data, it appears to be populated *via* a different mechanism.

Chapter 5

Conclusions

5.1 Summary of Experimental Data

The heavy ion plus 15 MeV γ coincidence data from the experimental runs is evidence of the one proton transfer reaction on ^{11}B, forming ^{12}C in the 15.11 MeV excited state. The two observed transitions, with different Q-values, are interpreted as giving $^{12}C_{gs}$+$^{12}C^{*}_{15.11}$ and $^{12}C^{*}_{4.44}$+$^{12}C^{*}_{15.11}$ in the exit channel, and indicate the mixed ground state structure of ^{13}N, *ie*

$$\alpha|^{12}\mathrm{C}(0^{+}) \otimes 1\mathrm{p}_{\frac{1}{2}}\rangle + \beta|^{12}\mathrm{C}(2^{+}) \otimes 1\mathrm{p}_{\frac{3}{2}}\rangle$$

Absolute cross sections have been obtained for each of the three experimental runs, without the need for normalising the data sets with respect to each other. The first and third runs, performed at 29.5 MeV, overlap slightly in the range of angles covered, and the data match well, confirming the independent normalisation factors. The reaction cross sections are characteristic of a one step, quasi-elastic direct reaction, suggesting that the excited carbon core nature of one of the exit channels is due to the structure of ^{13}N itself, rather than possible inelastic processes that might excite a ground state carbon into the 2^{+} state at 4.44 MeV.

5.2 Comparing Experiment and Theory

The DWBA calculations described in Chapter 4, initially using a plausible potential suggested by ^{12}C+^{11}B scattering, have only moderate success in reproducing the measured cross sections for the 0^+ transition at both energies for which data was taken, and rather poorer agreement for the 2^+ transition. Small adjustments, such as larger diffuseness or radius parameters, to the potential fail to produce a good fit to the current data.

Arbitrary changes to the optical potential should be treated with caution, however, and it would be preferable to explain the smooth decrease in cross section in terms of the reaction mechanism or with new optical parameters which can be justified in physical terms. The work of Liu *et al* [77] and references therein discuss the differential cross sections of the elastic transfer ^{13}C(^{12}C,^{13}C)^{12}C, which exhibit a lack of structure similar to that measured in the present work. Several possible explanations of this were put forward at the time by Dar [78, 79]:

1. Mixing of transferred angular momenta, due to configuration mixing in the initial and final states, or contributions from other processes.

2. Recoil (of the donor core nucleus), often neglected in early DWBA codes, damping out oscillations in the angular distributions [80].

3. Angular momentum mismatch (*cf* Q-matching, [29,30]), especially for high l transfer and large negative Q-values.

Items 2 and 3 can be discounted as explanations for the lack of structure in the angular distributions measured in the present work; the code `fresco` incorporates recoil, the transfer reaction on ^{11}B corresponds to $l = 0$, and the Q-values are only -1.1 and -5.5 MeV. This leaves item 1 as a possibility still to be considered if adjustments to the optical potential fail to reproduce the measured cross sections.

However, it turns out that a very much shallower potential (with larger radius and diffuseness) gives a better fit to the 0^+ transition at 29.5 MeV, in particular reducing the prominent diffraction features in the predicted cross sections, which are absent from the measured data. A similar system, ^{13}N+^{12}C, at a similar energy, also shows rather featureless cross sections at forward angles, and can also be described with a shallow optical potential (although not as shallow as the ones used here). This is perhaps small encouragement to believe the validity of the agreement obtained with the present data and potentials. The fact that another (slightly different) shallow complex potential reproduces the data reasonably well for both the 0^+ and the 2^+ transitions at the higher beam energy, when the 29.5 MeV cross sections for the 2^+ state are badly underestimated by the calculations, perhaps suggests that the reaction mechanism that is at work here is different at the lower energy.

5.3 Future Work

One possible direction in which to take this work in the future would be to attempt to obtain a more complete family of optical potentials that describe the transfer reaction. This process would be aided if elastic scattering data could be obtained; the standard route to potentials for inelastic scattering processes is to first model the elastic scattering. Computer codes exist which can quickly search for the best fit to elastic scattering, and levels of statistics are usually better in the elastic channel. It would also be interesting to examine the reactions of ^{13}N's mirror partner, ^{13}C, on ^{11}B. ^{12}B$_{\rm gs}$ is the $(J^\pi = 1^+, T = 1)$ analogue of ^{12}C$^*_{15.11}$, and the system ^{12}C$_{\rm gs}$+^{12}B$_{\rm gs}$ is very close in energy to ^{12}C$_{\rm gs}$+^{12}C$^*_{15.11}$. Elastic scattering data would also be useful; following the example of Liénard *et al* [25], potentials for ^{11}B(^{13}C,^{13}C) would be a good starting place for modelling the reactions of ^{13}N on ^{11}B, assuming that those potentials would not be very different for the mirror pair of nuclei, but also bearing in mind that the ^{13}N data seemed to require a

shallower imaginary potential. The kind of very shallow potential with $V_0 \approx 5$ that provided a better fit to the transfer to $^{12}C_{0^+}$ could perhaps also be applied to the reactions of $^{12}C+^{11}B$; the various published fits use values $V_0 = 50$ or 100, and there is clearly an ambiguity in the parameters of the optical potential. What kind of ambiguity this represents, and whether it might be consistent with very shallow potentials, is open to question, though.

The fact that different potentials seem to be required for the reaction at the higher beam energy suggests that an energy dependent form is appropriate here; clearly, though, data at a range of beam energies are required so that a firm conclusion about how the parameters would vary can be reached. In obtaining the potentials for the 45 MeV data, the parameters were simply varied randomly; the only correlation or reference to the fit at 29.5 MeV was that the value of V_0 was held constant. In this context, results for $^{12}C+^{11}B$ and $^{13}N,^{13}C+^{12}C$ at various beam energies would also be of interest to explore the possible systematics of the energy dependence in this mass region. It is also interesting to note the results of Liu *et al* [77]; optical model potential fits are obtained for $^{12}C+^{11}B,^{13}C$ and $^{14}N+^{11}B$ elastic scattering at various energies (table 5.1). These parameters suggest an energy dependence in the optical potential for $^{14}N+^{11}B$, although when interpreting these fits and their energy dependence, note must be made of which parameters were held constant during the search for the best fit to the data. Similarly, though, the fit of Liu *et al* to $^{12}C+^{13}C$ has a similar depth to the Liénard fit (which is for a lower energy), but a somewhat different geometry.

Another avenue that is worth pursuing is that of resonant effects in the exit channel, as mentioned in the previous chapter. Aside from the goal of explaining the transfer reaction cross sections, such an investigation would be of interest in itself, since the work published to date on molecular resonances in $^{12}C+^{12}C$ systems has used carbon on carbon in the entrance channel. If the width and position of such a resonance were to be measured, the use of thinner targets would be required, in order to obviate the problem of the effective width of the

#	V_0	r_{0r}	a_r	W_0	r_{0i}	a_i	System	
	(MeV)	(fm)		(MeV)	(fm)			E_{lab}
1	100*	0.80	0.985	8.30	1.46	0.62	^{14}N+^{11}B	40 MeV
2	50*	1.01	0.95	25.0*	1.32	0.60*		40 MeV
3	100*	0.90	0.85	10.85	1.39	0.49		74 MeV
4	50*	0.86	1.11	25.0*	1.30	0.50*		74 MeV
5	100*	1.02	0.78	9.64	1.41	0.47		113 MeV
6	50*	1.04	0.74	25.0*	1.40	0.45*		113 MeV
7	100*	1.02	0.70	26.0	1.10	0.44	^{12}C+^{11}B	87 MeV
8	100*	1.02	0.48	20.3	1.23	0.70	^{12}C+^{13}C	87 MeV
9	50*	0.95	0.70	25.0*	1.18	0.53		87 MeV

*quantity held constant during the search for a fit

Table 5.1: *Optical potentials from Liu* et al

projectile energy, due to energy loss in the target. This requirement would make the experiment quite difficult to carry out successfully, given the low currents available with radioactive beams.

Repeating the experiments at a range of beam energies would allow the investigation of the apparently energy-dependent nature of the optical potentials that were used here to reproduce the 0^+ data. The large gap in the measured cross sections at 45 MeV, due to the gap between the LEDA and Lampshade detectors should be filled, and measurements at backward angles would also be of interest, in order to further test the success of the calculations in reproducing the experimental data.

5.4 Summary

The transfer reaction ^{11}B(^{13}N,^{12}C)^{12}C has been clearly identified with two states in ^{12}C$^{(*)}$+^{12}C* being distinguished, and absolute cross sections have been obtained

for each transition for centre of mass energies 12.6 MeV and 20.0 MeV. The gamma de-excitation of the $^{12}C^*$ (15.11 MeV) has provided a signature for the reaction which allows transfer events to be clearly identified, with almost no background.

It has been attempted to interpret the origin of the two observed transitions in terms of configuration mixing in the ^{13}N ground state. DWBA calculations have reproduced the angular distributions for the ground state transition reasonably successfully, by use of very shallow optical potentials, which appear to be energy dependent. The cross section for the transition to the 2^+ state in $^{12}C^*$ at the lower beam energy is by comparison well underestimated by the calculations, however, suggesting that some mechanism other than a direct one-step transfer contributes to the reaction strength in this case. The same transition at $E_{lab} = 45$ MeV is reproduced rather better with this model, in form as well as in magnitude.

Core excitation is one possibility for an alternative mechanism that might populate the 2^+ state, although we would imagine that this would compete with the direct transfer to the ground state, and the agreement between the code's predictions and experiment would be expected to be poor for both the identified final states. Coupling between the 0^+ and 2^+ states in the exit channel is expected to be small, moreover [24]. Another possibility is that the experiment as performed in the present work has happened to hit a resonance in $^{12}C^*+^{12}C^*$. It is suggested that future work should investigate this possibility further, by repeating the experiment at a range of energies around 11 MeV in the centre of mass.

Appendix A

Kinematics and Energy Loss

At the beam energies used in these experiments, and with the thickness of target used, energy loss in the target becomes a significant factor in the calculations performed during the analysis of the data. The low yield of the radioactive beam makes it necessary to use much thicker targets than would usually be used in heavy-ion research, so that a reasonable level of statistics can be obtained. Since the reactions being measured can take place at any point inside the target, with a correspondingly varying energy loss experienced by the beam particles, the recorded data sample events that take place with a range of projectile energies. Furthermore, energy loss of the reaction products in the target will also have an effect on what the detectors 'see.' Another factor to be considered is the thin dead layer on the surface of the silicon detectors, from which charge is not collected and which therefore makes its own small contribution to the difference between the original energy of the reaction products and the measured energy. This appendix describes some of the corrections to the calculations that are made necessary by the stopping power of 800 $\mu g\,cm^{-2}$ (or 3.2 μm) of boron.

A.1 Two Body Kinematics

When interpreting the singles particle spectra or the particle-gamma coincidence spectra, it is necessary to know where the peaks for elastic scattering or the transfer reaction should be. The kinematics of elastic scattering or a two-body inelastic process are straightforward [81]; for beam energy E_1, projectile mass M_1, target mass M_2, products M_3 and M_4 and Q-value Q we have, in the lab frame:

$$E_3 = B\left[\cos\theta \pm \left(\frac{D}{B} - \sin^2\theta\right)^{1/2}\right]^2 \tag{A.1}$$

$$B = \frac{E_1 M_1 M_3}{(M_1 + M_2)(M_3 + M_4)}$$

$$D = \frac{M_2 M_4}{(M_1 + M_2)(M_3 + M_4)}\left[1 + \frac{M_1 Q}{M_2(E_1 + Q)}\right]$$

which for elastic scattering ($M_3 = M_1, M_4 = M_2$) simplifies to

$$E_3 = E_1\left(\frac{M_1}{M_1 + M_2}\right)^2\left\{\cos\theta \pm \left[\left(\frac{M_2}{M_1}\right)^2 - \sin^2\theta\right]^{1/2}\right\}^2 \tag{A.2}$$

Equation A.2 contains two solutions; however, the solution given by using the minus sign can in practice be disregarded in this case since it corresponds to energies below threshold for the detector apparatus.

This θ dependence of the energy holds for the ideal case of a very thin target, but in practice it will be affected by energy loss; 800 μg cm^{-2} of boron would degrade a 29.5 MeV ^{13}N beam by $\Delta E \approx 4$ MeV (at 45 MeV the figure is 3 MeV).

One solution might simply be to subtract an amount ΔE from the calculated energies, or to perform the calculation for a beam energy $E - \Delta E$. However, a more satisfactory approach is to average over the thickness of the target when estimating the effect of energy loss; the scattering (or reaction) could take place at any depth in the target, and for a large enough scattering angle the energy loss for the two extremes will be rather different. Taking the average of the two extreme

cases, or a number of intermediate scattering points gives a good estimate of the expected energy. Figure A.1 shows the results for elastic scattering of ^{13}N with various target masses, in 800 μg cm^{-2} of boron, and for the transfer reaction to the two states in ^{12}C. This figure also includes a correction made for the energy loss in the detector's dead layer—an amount ΔE_{dead} is subtracted to give the energy we would expect to measure, assuming a dead layer thickness of 1 μm of aluminium.

Strictly speaking, two body kinematics does not apply to the transfer reaction, since there is a γ-photon involved as well. However, this has been neglected, since a 15 MeV photon has only 2% of the momentum of a 20 MeV ^{12}C nucleus.

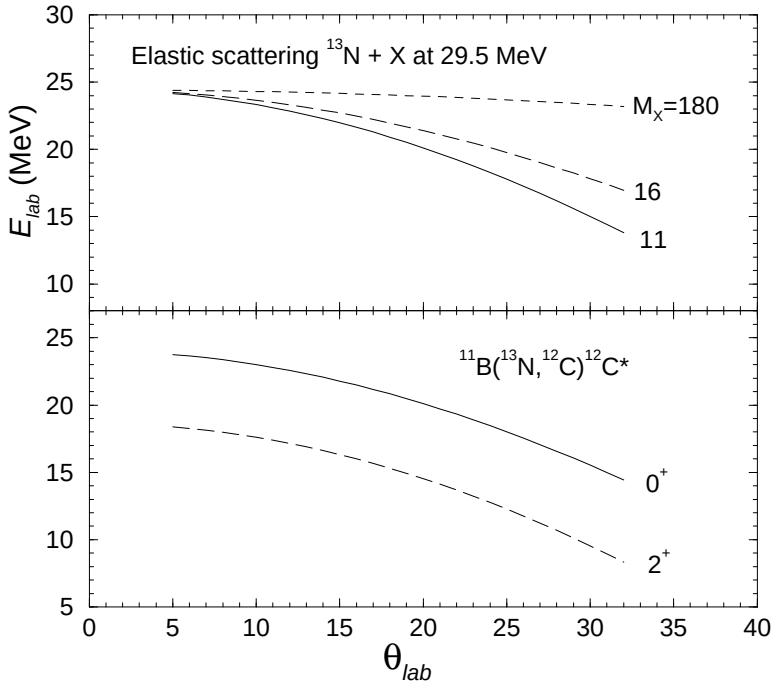

Figure A.1: *Elastic scattering and transfer reaction with energy loss*

In these experiments we have primarily used the detection of a heavy ion in coincidence with a 15 MeV gamma ray to identify the transfer reaction. However, with the Lampshade array it is sometimes possible to detect both the beam-like and the recoil carbons. There are two restrictions which limit the cases in which this is possible. One is the range of angles covered by the detectors, and the

other is energy loss in the target. At low energies, below about 4 MeV, most of the carbons will be stopped in the target, so when extracting the 15 MeV gamma coincidence events, sorted spectra should contain events with Lampshade multiplicity one and two. Figure A.2 shows the angles for the two carbons in each transition, for both beam energies.

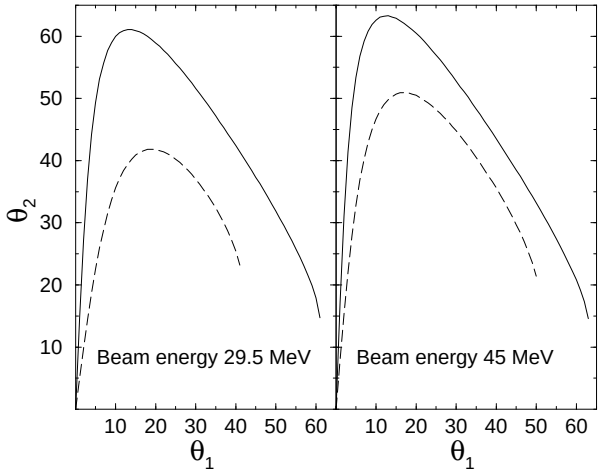

Figure A.2: *Two body kinematics of the transfer reaction*
Solid lines: 0^+ transition. Dashed lines: 2^+ transition.
Angles are in the lab frame.

The calculations show that if one carbon is scattered into the array used in the first run (14°–32°) the second would miss because the opening angle is always too big—we can only see one carbon at a time in the data from the first experiment.

With the LEDA-Lampshade detector configuration, however, it is possible that both carbons will appear in the Lampshade, which covers 21°–69°. LEDA-LEDA and LEDA-Lampshade coincidences are ruled out, however; all the observable events are in the Lampshade, because in the second and third runs the plane LEDA covered only 6°–14°.

A.2 `fresco` Runs

The energy loss in the target also affects the `fresco` calculations, because the beam energy is one of the input parameters, and the experimental data will contain contributions from reactions occurring at energies between E and $E - \Delta E$. Since here we are interested in cross sections and not final energies, the solution is to run the code for a number of energies between E and $E - \Delta E$, and to take the average of the distributions obtained. The cross sections generated by the code can be strongly dependent on the projectile energy, particularly in the case of the 2^+ transition at 29.5 MeV (see fig. A.3).

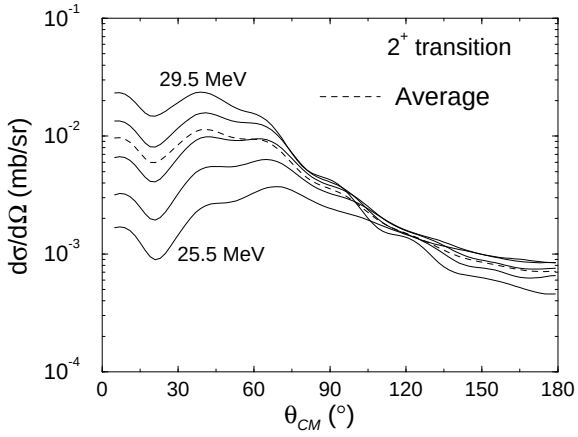

Figure A.3: *Effect of target thickness on* `fresco` *cross sections*

Bibliography

[1] G. Vancraeynest *et al*, Nucl. Phys. **A616** (1997), 107c.

[2] C.R. Bain *et al*, Phys. Lett. B **373** (1996), 35.

[3] P.E. Haustein, Nucl. Phys. **A616** (1997), 469c.

[4] H. Geissel *et al*, Ann. Rev. Nucl. Part. Sci. **45** (1995), 163.

[5] E.H.S. Burhop *et al*, Nucl. Phys. **A132** (1969), 625.

[6] B. Blank *et al*, Z. Phys. A **343** (1992), 375.

[7] M.V. Zhukov *et al*, Nucl. Phys. **A539** (1992), 177.

[8] T. Suzuki *et al*, Phys. Rev. Lett. **75** (1995), 3241.

[9] W.X. Wen *et al*, High Energy Phys. and Nucl. Phys. **20** (1996), 101.

[10] L. Chulkov *et al*, Nucl. Phys. **A603** (1996), 219.

[11] A.A. Korsheninnikov *et al*, Nucl. Phys. **A617** (1997), 45.

[12] K. Riisager, Rev. Mod. Phys. **66** (1994), 1105.

[13] P.G. Hansen *et al*, Ann. Rev. Nucl. Part. Sci. **45** (1995), 591.

[14] M.V. Zhukov and I.J. Thompson, Phys. Rev. C **52** (1996), 3505.

[15] C. Borcea *et al*, Nucl. Phys. **A616** (1997), 231c.

[16] S. Blatt *et al*, Phys. Rev. C **30** (1984), 423.

[17] P. Corvisiero *et al*, Nucl. Phys. **A526** (1991), 141.

[18] A. Zucchiatti *et al*, Nucl. Phys. **A575** (1994), 317.

[19] F. Ajzenborg-Selove, Nucl. Phys. **A523** (1991), 1.

[20] S. Cohen and D. Kurath, Nucl. Phys. **73** (1965), 1.

[21] S. Cohen and D. Kurath, Nucl. Phys. **A101** (1967), 1.

[22] M.K. Singham, Nucl. Phys. **A460** (1986), 597.

[23] M.K. Singham, Phys. Rev. Lett. **54** (1985), 1642.

[24] J.A. Christley F. Nunes and J.A. Tostevin, *Transfer Reaction Calculations for* $^{11}B(^{13}N,^{12}C)^{12}C^{*}(15.11\ MeV)$, Internal Report, Surrey University, February 1995.

[25] E. Liénard *et al*, Phys. Rev. C **52** (1995), 775.

[26] W. von Oertzen, Nucl. Phys. **A148** (1970), 529.

[27] W. von Oertzen and H.G. Bohlen, Phys. Rep. **19C** (1975), 1.

[28] B. Imanishi and W. von Oertzen, Phys. Rep. **155** (1987), 29.

[29] D. Brink, Phys. Lett. **B40** (1972), 37.

[30] P.J. Siemens *et al*, Phys. Lett. **B36** (1971), 24.

[31] R. Bass, *Nuclear Reactions With Heavy Ions*, Springer-Verlag, 1980.

[32] D. Darquennes *et al*, Nucl. Instr. Meth. Phys. Res. B **47** (1990), 311.

[33] D. Darquennes *et al*, Phys. Rev. C **42** (1990), R804.

[34] P. Decrock *et al*, Nucl. Instr. Meth. Phys. Res. **B58** (1991), 252.

[35] G. Hall, Rep. Prog. Phys. **57** (1994), 481.

[36] G.F. Knoll, *Radiation Detection and Measurement*, Wiley, 1979.

[37] Micron Semiconductors Ltd, Lancing, UK.

[38] T. Davinson *et al*, Nucl. Instr. Meth. Phys. Res. **A288** (1990), 245.

[39] S.L. Thomas *et al*, Nucl. Instr. Meth. Phys. Res. **A288** (1990), 212.

[40] S. Majewski and D. Anderson, Nucl. Instr. Meth. Phys. Res. **A241** (1985), 76.

[41] M. Murashita *et al*, Nucl. Instr. Meth. Phys. Res. **A243** (1986), 67.

[42] M. Laval *et al*, Nucl. Instr. Meth. **206** (1983), 169.

[43] D.F. Anderson *et al*, Nucl. Instr. Meth. Phys. Res. **217** (1983), 217.

[44] K. Wisshak and F. Kappeler, Nucl. Instr. Meth. Phys. Res. **A227** (1984), 91.

[45] C. Agodi *et al*, Nucl. Instr. Meth. Phys. Res. **A269** (1988), 595.

[46] T. Matulewicz *et al*, Nucl. Instr. Meth. Phys. Res. **A289** (1990), 194.

[47] P. Schotanus *et al*, Nucl. Instr. Meth. A **238** (1985), 564.

[48] S. Kobuta *et al*, Nucl. Instr. Meth. Phys. Res. **A289** (1990), 253.

[49] Wilfried Galster, *Private communication.*

[50] A. Musumarra *et al*, Nucl. Instr. Meth. Phys. Res. **A370** (1996), 558.

[51] David Brightly, Daresbury Laboratory, UK.

[52] G.D. Lafferty and T.R. Wyatt, Nucl. Instr. Meth. Phys. Res. **A355** (1995), 541.

[53] J. Kemmer and R. Hoffmann, Nucl. Instr. Meth. **176** (1980), 543.

[54] I.S. Dmitriev and V.S. Nikolaev, Sov. Phys. JETP **20** (1965), 409.

[55] R.B. Firestone and V.S. Shirley (eds.), *Table of Isotopes*, 8 ed., Wiley, 1996.

[56] Armstrong and Chandler, ORNL 4869, 1973.

[57] I.J. Thompson, FRESCO users' manual, available from the author, 1995.

[58] I.J. Thompson, Comp. Phys. Comm. **7** (1988), 167.

[59] P.L. Kerr *et al*, Phys. Rev. C **54** (1997), 1267.

[60] P.D. Kunz, Program CHUCK3 (University of Colorado, 1978), extended version by J.R. Comfort (University of Pittsburgh, 1980).

[61] G.R. Satchler, *Direct Nuclear Reactions*, Oxford University Press, 1983.

[62] M.E. Brandan and K.W. McVoy, Phys. Rev. C **55** (1997), 1362.

[63] P.E. Hodgson, *Nuclear Reactions and Nuclear Structure*, Oxford University Press, 1971.

[64] U. Voos *et al*, Nucl. Phys. **A135** (1969), 207.

[65] I. Tanihata *et al*, Phys. Rev. Lett. **55** (1985), 2676.

[66] P. Dück *et al*, Nucl. Phys. **A251** (1975), 344.

[67] W. von Oertzen *et al*, Phys. Lett. **26B** (1968), 291.

[68] D. Baye. *et al*, Nucl. Phys. **A289** (1977), 511.

[69] D. Baye, Nucl. Phys. **A460** (1986), 581.

[70] B. Imanishi *et al*, Phys. Rev. C **55** (1997), 1946.

[71] D.A. Bromley *et al*, Phys. Rev. Lett. **4** (1960), 365.

[72] E. Almqvist *et al*, Phys. Rev. Lett. **4** (1960), 515.

[73] K.A. Erb and D.A. Bromley, *Heavy Ion Resonances* in *Treatise on Heavy Ion Science vol. 3,* ed. D.A. Bromley, Plenum Press, 1985.

[74] T.M. Cormier and B.R. Fulton, Phys. Rev. C **22** (1980), 565.

[75] S. Szilner *et al*, Phys. Rev. C **55** (1985), 1312.

[76] Alessia Di Pietro, *Private communication.*

[77] M. Liu *et al*, Nucl. Phys. **A165** (1971), 118.

[78] A. Dar, Phys. Rev. **139** (1965), 1193.

[79] A. Dar *et al*, Phys. Rev. Lett. **15** (1965), 1036.

[80] L.R. Dodd and K.R. Greider, Phys. Rev. **180** (1969), 1187.

[81] Marion and Young, *Nuclear Reaction Analysis: Graphs and tables*, North Holland Pub. Co., 1968.